



## Dipole collapse and reversal precursors in a numerical dynamo

Peter Olson<sup>a,\*</sup>, Peter Driscoll<sup>a</sup>, Hagay Amit<sup>b</sup>

<sup>a</sup> Department of Earth & Planetary Sciences, Johns Hopkins University, 3400 North Charles St., Baltimore, MD 21218, USA

<sup>b</sup> Equipe de Géomagnétisme, Institut de Physique du Globe de Paris (Institut de Recherche associé au CNRS et à l'Université Paris 7), 4 Place Jussieu, 75252 Paris Cedex 05, France

### ARTICLE INFO

#### Article history:

Received 23 May 2008

Received in revised form 21 October 2008

Accepted 9 November 2008

#### Keywords:

Dipole collapse  
Polarity reversals  
Dynamo models  
Geodynamo  
Earth's core  
Geomagnetic field  
Butterfly diagrams

### ABSTRACT

Precursors to extreme geomagnetic field changes are examined in a numerical dynamo with a reversing dipolar magnetic field. A dynamo model with compositional convection in a rotating spherical shell produces a strongly dipolar external magnetic field over 6 Myr of simulated paleomagnetic time, with stable polarity epochs and occasional dipole collapses, some of which result in polarity reversals or dipole axis excursions. We analyze the model behavior during two dipole collapses, one that leads to a polarity reversal and one that does not, focusing on observable precursors. Reversed magnetic field induced in the dynamo interior by intermittent convective variability is the primary cause of dipole collapse. Spots of reversed magnetic flux emerge on the outer boundary at an early stage, then re-emerge with greater intensity at the height of the collapse. The energy in the external field cascades to higher harmonics as these reversed patches appear. Butterfly diagrams showing the reversed and normal flux contributions to the axial dipole reveal poleward migration of the patches during dipole collapse. Axial dipole reduction by precursory reversed flux is several times larger in the reversing case, compared to the non-reversing case. A butterfly diagram of the geomagnetic field since 1840 shows high latitude reversed flux emerging on the core–mantle boundary. Although the reversed geomagnetic flux is presently too weak to be labeled a reversal precursor, it is consistent with early stage dipole collapse in the dynamo model.

© 2008 Elsevier B.V. All rights reserved.

### 1. Introduction

The geomagnetic field has a history of large amplitude and sometimes rapid changes in the dipole strength and direction, including polarity reversals and excursions. According to the marine paleomagnetic record, polarity reversals and excursions typically coincide with episodes of very low dipole field strength (Valet, 2003), events referred to in this paper as dipole collapses. The duration of geomagnetic dipole collapses are evidently variable, typically lasting some tens of thousands of years, during which time the geomagnetic dipole moment falls by a factor of 2–5 compared to its time average value (Valet et al., 2005). Superficially, these dipole collapses appear to be similar to the low frequency geomagnetic intensity fluctuations found throughout the recent marine paleomagnetic record (Lund et al., 2006; Tauxe and Yamazaki, 2007) except that they involve more extreme dipole strength changes and often result in a polarity reversal or an excursion. The directional instability of the field in a reversal or an excursion is typically shorter than the preceding dipole collapse, and lasts about 6–10 kyr on average (Glatzmaier and Coe, 2007) although its duration depends on the latitude of the observation

(Clement, 2004). Following the reversal, the dipole recovers in the new polarity over the next few tens of thousands of years, sometimes reaching a higher intensity than it had prior to collapse (Bogue and Paul, 1993; Valet and Herrero-Bervera, 2003).

In the recent historical times the geomagnetic dipole moment has been decreasing, from about  $85 ZAm^2$  ( $Z \equiv 10^{21}$ ) in 1840 to about  $77 ZAm^2$  in 2005 (Jackson et al., 2000; Maus et al., 2005). This is approximately 10–12 times the rate of free Ohmic decay of a simple dipole field in the core (Olson and Amit, 2006) and therefore qualifies as rapid change for the geodynamo. It has often been conjectured that the present-day geodynamo might be in the early stage of a dipole collapse (McDonald and Gunst, 1968; Constable and Korte, 2006; Olson and Amit, 2006). Indeed there are good reasons to anticipate that the historical rate of decrease will continue. According to the POMME-4.0 main field model (<http://geomag.org/models/pomme4.html>) the dipole moment decrease at epoch 2004 is equivalent to 5.4% per century, about the historical average, while the IGRF 2005 main field (<http://www.ngdc.noaa.gov/AGA/vmod/>) includes a dipole moment decrease equivalent to about 5% per century. Additional evidence for a sustained decrease comes from the growth and generally poleward migration of large patches of reversed magnetic field on the core–mantle boundary that have contributed substantially to the historical dipole moment drop (Gubbins, 1987; Olson and Amit, 2006). Global archeomagnetic models indicate the geomagnetic dipole moment exceeded  $90 ZAm^2$  within the past 2 kyr

\* Corresponding author.

E-mail address: [olson@jhu.edu](mailto:olson@jhu.edu) (P. Olson).

(Korte and Constable, 2005) and some regional archeomagnetic data indicate a value in excess of  $100 \text{ ZAm}^2$  during this time (Yang et al., 2000).

## 2. Dipole collapse and reversal in numerical dynamos

Many numerical dynamos exhibit rapid magnetic field changes, including large-amplitude reductions in dipole intensity that fit our definition of collapse events. Spontaneous polarity reversals and excursions sometimes follow dipole collapses in these models (Glatzmaier and Roberts, 1995; Kutzner and Christensen, 2002; Wicht and Olson, 2004; Wicht, 2005; Takahashi et al., 2005, 2007; Olson, 2007; Aubert et al., 2008b; Rotvig, submitted for publication; Nishikawa and Kusano, 2008). The transition fields produced by reversing dynamo models sometimes conform to the gross behavior of the geomagnetic field during reversals as described above, but not always. Because the reversal processes in these models are typically quite complex, it has proven difficult to isolate their fundamental causes, and questions remain about whether the reversal mechanisms in dynamo models are applicable to the reversal mechanisms in the core. There is, however, a general consensus on the basic sequence of events in a dynamo model reversal and which control parameters affect them.

Attributes common to most dynamo model reversals include a prolonged interval of dipole strength decrease, the dipole collapse, followed by a shorter directional transition in which the dipole axis migrates from one hemisphere to the other, ending with a recovery phase when the dipole axis stabilizes near the opposite pole and the dipole moment strengthens. Similar to the paleomagnetic observations, the apparent duration of a dynamo model reversal or excursion varies with site location (Wicht, 2005).

The likelihood for polarity reversals increases with the amount of magnetic variability in dynamo models, and the amount of magnetic variability depends on the external control parameters in different ways. Kutzner and Christensen (2002) show that a transition from non-reversing to reversing dynamos occurs as the Rayleigh number of the convection is increased (assuming the other control parameters are fixed), with more frequent reversals occurring at higher Rayleigh number where the magnetic fluctuations are larger. Olson (2007) finds a transition from non-reversing to reversing dynamos above a certain Rayleigh number, where the ratio of the dipole strength fluctuations to the time average dipole strength exceeds a certain value. Rotvig (submitted for publication) also finds a Rayleigh number threshold for reversals, and attributes reversals to the transition from strongly dipolar to weaker multi-polar field dynamo states.

Factors other than the Rayleigh number are known to affect dynamo model reversals. Nishikawa and Kusano (2008) show that increasing the magnetic Prandtl number promotes the weak field transition and favors reversals in compressible dynamos. Planetary rotation evidently has the opposite effect on reversals, according to dynamo models. Increasing rotation rate (i.e., decreasing the Ekman number) reduces magnetic variability and tends to inhibit reversals (Driscoll and Olson, submitted for publication), although reversals have been found in very low Ekman number dynamos when the Rayleigh number is sufficiently large (Takahashi et al., 2005, 2007).

Finally, boundary conditions have some control over dynamo behavior, particularly thermal heterogeneity at the outer (i.e. core–mantle) boundary. Patterns of core–mantle boundary heat flow heterogeneity that match the internal symmetry pattern of convective heat transport in the core promote dynamo stability and make reversals less frequent, compared to core–mantle boundary heat flow patterns that differ from this symmetry (Glatzmaier et al., 1999). The transition field structure is modified by the boundary heterogeneity, so that the apparent path of the geomagnetic

pole during the polarity change may show a longitudinal bias (Coe et al., 2000; Kutzner and Christensen, 2004). The magnetic field can also be locked to the boundary thermal heterogeneity when convection is slightly supercritical (Gubbins et al., 2007; Willis et al., 2007).

Dynamo models are equivocal as to the preferred site in the core where reversals begin. Wicht and Olson (2004) found that reversed flux is generated both inside and outside the tangent cylinder in a high Ekman number (slowly rotating) dynamo, with the reversed flux outside the tangent cylinder precipitating the reversal. Takahashi et al. (2007) find dipole collapses and reversals in low Ekman (rapidly rotating) dynamos also begin with reversed magnetic flux generated at low latitudes, outside of the tangent cylinder. In contrast, Aubert et al. (2008b) and Rotvig (submitted for publication) find a mixed behavior, with reversals and excursions initiated by reversed flux generated both outside and inside the tangent cylinder.

Some of the variety in reversal processes reflects the variety of dynamo types. Magnetic variability in reversing dynamos is often associated with changes in the flow, in the form of intermittent variability and symmetry changes in the convection. For example, Nishikawa and Kusano (2008) attribute reversals to intermittent increases in the part of the flow that is antisymmetric with respect to the equator. However, there are reversing dynamo models in which the total kinetic energy remains nearly constant and the variability is almost entirely in the magnetic energy. For example, large amplitude variability in the magnetic energy and periodic polarity reversals are common in dynamo models of the  $\alpha\omega$ -type, even in cases where the kinetic energy variability is small (Wicht and Olson, 2004). In this type of dynamo, the  $\omega$ -effect derived from the large-scale thermal wind flows induces magnetic oscillations in which the poloidal and toroidal parts of the magnetic field fluctuate out of phase, resulting in a kind of kinematic dynamo wave with quasi-periodic magnetic secular variation, regularly spaced polarity changes, and nearly uniform duration of the polarity chrons. A defining property of these wave-like dynamos is the concentration of secular variation at discrete dynamo wave frequencies. Although dynamo waves probably contribute to the geomagnetic secular variation, the fact that the geomagnetic secular variation energy is distributed in a broad-band rather than a line spectrum (Constable and Johnson, 2005) argues against a dynamo wave interpretation of geomagnetic dipole collapses. Accordingly, we restrict our attention in this study to a dynamo model in which the low frequency poloidal and toroidal magnetic field energy variations are in phase, their frequency spectra are broad-band, and the duration of the polarity chrons is irregular. In these dynamos the low frequency variability in the magnetic field is out of phase (inversely correlated) with the low frequency variability in the flow, due to the action of the Lorentz force (Olson, 2007).

The connection between observable magnetic field structures on the core boundary and internal dynamo processes is crucial for understanding dipole collapses and polarity reversals. Aubert et al. (2008b) identify two classes of magnetohydrodynamic structures that play important roles in dynamo variability. One class are axial (i.e., rotationally aligned) vortices with concentrated axial magnetic fields in their cores. These structures tend to be relatively long-lived and are particularly evident in equatorial sections at high magnetic Reynolds number conditions. The polarity of the magnetic fields in these vortices largely determines the overall polarity of the dynamo. In this paper, we refer to these concentrated internal magnetic fields as magnetic flux ropes. Axial magnetic ropes evolve on a relatively long time scale, in concert with the low frequency dipole strength variations, and are the critical elements of our dynamo model.

The other class of magnetohydrodynamic structures important to dipole collapse and reversals are transient upwellings that advect

bent magnetic field lines from the deep interior toward the surface, called magnetic upwellings by Aubert et al. (2008b). Reversed flux patches form where magnetic upwellings impinge on the dynamo outer boundary (Wicht and Olson, 2004). There are also diffusive mechanisms for reversed flux generation (Bloxham, 1986), but magnetic upwellings produce them more rapidly, on the time scale of the convection (Takahashi et al., 2007). The convective surges identified as triggering agents for polarity reversals by Sarson and Jones (1999) may consist of such magnetic upwellings. Magnetic upwellings are most important when the overall pattern of the convection is rapidly evolving, compared to when it is changing slowly. Our model shows intermittent variability in convection, although it is due to fluctuations in the axial vortices, rather than formation of new magnetic upwellings.

An important question that dynamo modeling has not resolved is whether it is possible to predict if a relatively short-term geomagnetic field change, like the present-day dipole decrease, is likely to develop into a full-scale dipole collapse or even a polarity reversal. In other words, are there observable geomagnetic precursors for dipole collapses and reversals? Since most dynamo model reversals occur when the dipole is already weakened, sustained dipole decrease is an obvious precursor. However it is not a particularly useful predictor. Only a small minority of the dipole decreases in the paleomagnetic secular variation record led to collapses and polarity reversals (Valet et al., 2005) so that a decreasing dipole moment does not reliably indicate that a full-scale dipole collapse is imminent. A collapse interpretation for today's field is additionally problematic because, in spite of its recent decrease, the present-day geomagnetic dipole may actually be stronger than average (Constable and Korte, 2006).

The emergence of reversed magnetic flux on the core–mantle boundary has been interpreted as a symptom of polarity change (Cox, 1975; Gubbins, 1987). Reversed flux on the core–mantle boundary tends to evolve rapidly with time (Olson and Amit, 2006), consistent with a rapidly fluctuating convection pattern. Rapid fluctuation of the convective pattern may favor mixing over regeneration of the large-scale internal magnetic field, so we might anticipate that the appearance of large amounts of reversed boundary flux might signal a dipole collapse.

In this paper, we focus on shorter-term, potentially observable precursory effects associated with dipole collapse. We compare two dipole collapses from the same dynamo model, one producing a polarity reversal, the other producing only a relatively minor displacement of the dipole axis. In both cases the dipole collapse is related to intermittent high frequency dynamo variability and some loss of symmetry in the velocity field, and is marked by the growth of a reversed flux rope in the equatorial plane, reversed flux precursors on the outer boundary, and modification of the external field spectrum toward higher wave number components. Butterfly diagrams of the reversed flux and evolution diagrams of the external field spectrum are shown to be potentially useful diagnostics in forecasting dipole collapse and polarity reversal.

### 3. Dynamo model

The dynamo model solves the following dimensionless equations for conservation of momentum, mass and magnetic field continuity, buoyancy transport, and magnetic induction for convection and magnetic field generation in an electrically conducting fluid in a rotating, self-gravitating spherical shell:

$$E \left( \frac{\partial \mathbf{u}}{\partial t} + \mathbf{u} \cdot \nabla \mathbf{u} - \nabla^2 \mathbf{u} \right) + 2\hat{\mathbf{z}} \times \mathbf{u} + \nabla P = EPr^{-1}Ra \frac{\mathbf{r}}{r_o} \chi + Pm^{-1}(\nabla \times \mathbf{B}) \times \mathbf{B} \quad (1)$$

$$\frac{\partial \mathbf{B}}{\partial t} = \nabla \times (\mathbf{u} \times \mathbf{B}) + Pm^{-1} \nabla^2 \mathbf{B} \quad (2)$$

$$\frac{\partial \chi}{\partial t} + (\mathbf{u} \cdot \nabla) \chi = Pr^{-1} \nabla^2 \chi - 1 \quad (3)$$

$$\nabla \cdot (\mathbf{u}, \mathbf{B}) = 0 \quad (4)$$

where  $\mathbf{u}$ ,  $P$ ,  $\chi$  and  $\mathbf{B}$  are the fluid velocity, pressure perturbation, perturbation of the light element concentration, and magnetic induction, respectively,  $t$  is time,  $\mathbf{r}$  is the radius vector (all dimensionless), and  $E$ ,  $Pr$ ,  $Ra$  and  $Pm$  are the Ekman, Prandtl, Rayleigh and magnetic Prandtl numbers, respectively. The conservation of momentum (1) is the Boussinesq form of the Navier–Stokes equation in a spherical  $(r, \theta, \phi)$  coordinate system rotating at angular velocity  $\Omega \hat{\mathbf{z}}$  in which gravity increases linearly with radius. Eqs. (1)–(4) have been nondimensionalized using the shell thickness  $D$  as the length scale and the viscous diffusion time  $D^2/\nu$  as the time scale, where  $\nu$  is the kinematic viscosity. We use  $r_o$  and  $r_i$  to denote the dimensionless outer and inner boundary radii, respectively, and  $r_c$  to denote the dimensional outer radius, so that  $r_c = Dr_o$ . We choose  $r_i/r_o = 0.35$ , approximating the Earth's inner core boundary/core–mantle boundary radius ratio. The fluid velocity is scaled by  $\nu/D$  and the magnetic field by  $(\rho_o \Omega / \sigma)^{1/2}$ , where  $\rho_o$  is the mean fluid density and  $\sigma$  is its electrical conductivity. The light element concentration variable  $\chi$  is scaled by  $D^2 \dot{\chi}_o / \nu$ , where  $\dot{\chi}_o$  is the rate of change of the volume averaged light element concentration in the fluid  $\chi_o$ , and is assumed constant in time. The  $-1$  factor in (3) is just the scaled representation of  $-\dot{\chi}_o$  (Kutzner and Christensen, 2000). Boundary conditions for the composition variable are fixed light element concentration  $\chi = \chi_i$  at the inner boundary  $r = r_i$ , and zero light element flux  $\partial \chi / \partial r = 0$  at the outer boundary  $r = r_o$ . On both inner and outer boundaries the mechanical conditions are no-slip and electrical conditions are insulating.

Three of the control parameters in (1)–(4) have standard definitions:  $E = \nu / \Omega D^2$ ,  $Pr = \nu / \kappa$ , where  $\kappa$  is the diffusivity of the light elements, and  $Pm = \nu / \eta$ , where  $\eta = 1 / \mu_o \sigma$  is the magnetic diffusivity ( $\mu_o$  is magnetic permeability). In terms of our scaling, the Rayleigh number in (1) is

$$Ra = \frac{\beta g_o D^5 \dot{\chi}_o}{\kappa \nu^2} \quad (5)$$

where  $\beta = -1 / \rho \partial \rho / \partial \chi$  and  $g_o$  is gravity at the outer boundary.

Although (1)–(4) use viscous diffusion time scaling, we report our results in magnetic time, using the  $e$ -fold free decay time of a dipole field in a uniform conducting sphere with radius  $r_c$  as the basic time unit, which corresponds to about 20 kyr of paleomagnetic time. The ratio of this time scale to the viscous diffusion time scale  $D^2/\nu$  is given by

$$t_d = Pm \left( \frac{r_o}{\pi} \right)^2 \quad (6)$$

The corresponding dimensionless frequency is  $f_d = 1/t_d$ . In addition, we report the dynamo fluid velocities in magnetic Reynolds number units. The rms fluid velocity in magnetic Reynolds number units  $u_\eta$  is related to the velocity in (1)–(4) according to  $u = u_\eta / Pm$ . We report the magnetic field in terms of the dimensionless rms dipole intensity on the outer boundary  $B_d$ , the dimensionless rms total field intensity on the outer boundary  $B_o$ , and the dimensionless rms total internal field intensity  $B$ .

We choose a dynamo with  $Pr = 1$  for the Prandtl number,  $Pm = 20$  for the magnetic Prandtl number,  $E = 6.5 \times 10^{-3}$  for the Ekman number, and  $Ra = 1.9 \times 10^4$  for the Rayleigh number. The large magnetic Prandtl number provides a large magnetic Reynolds number, ensures strong magnetic field advection, a large Lorentz force, and favors a dipole-dominated magnetic field (Kutzner and Christensen, 2002). In a previous study, Olson (2007) investigated this type of dynamo over a wide range of Rayleigh numbers and

found  $Ra \simeq 8.8 \times 10^3$  for the Rayleigh number at dynamo onset, corresponding to a magnetic Reynolds number of  $u_\eta \simeq 40$ , chaotic dynamo behavior for  $Ra > 1.5 \times 10^4$ , with polarity reversals for  $Ra > 1.7 \times 10^4$ .

The dynamo code MAG used in this study is available at <http://www.geodynamics.org>. Originally developed by G. Glatzmaier, it is based on the semi-spectral method, with finite difference grid for the nonlinear terms and harmonic transforms for the linear terms. It has been previously benchmarked against standard dynamo solutions (Christensen et al., 2001). In this study we use 25 radial grid intervals with 23 Chebyshev polynomials and triangular spherical harmonic truncation at degree  $l_{\max} = 32$ . The truncation level of the spherical harmonics were chosen to ensure that the spectral power of magnetic energy attenuates by a factor one hundred or more from its peak  $l$ -value, and that the inner and outer boundary layers are well-resolved.

#### 4. Rationale for large Ekman number dynamo models

Dynamo models with low Ekman and Prandtl numbers are more directly applicable to convective process in the Earth's core because they better approximate the low viscosity of the outer core fluid. In particular, these models have energetic small scale motion (Glatzmaier, 2002; Takahashi et al., 2005, 2007, 2008; Christensen and Wicht, 2007; Kageyama et al., 2008) that is absent in models with larger values of these parameters, yet is probably important in the outer core (Loper, 2007). Since the Ekman and magnetic Prandtl numbers for the outer core are minute ( $10^{-13} - 10^{-9}$  and  $10^{-5} - 10^{-7}$ , respectively), it might seem that the smaller these parameters are, the more realistic the model. However, realism in geodynamo modeling involves an optimal combination of several control parameters, including  $E$  and  $Pm$  but also  $Ra$ ,  $Pr$ , appropriately scaled internal driving forces (i.e., chemical and thermal convection) and complex boundary conditions. Adopting extreme values for a subset of these parameters does not ensure the dynamo model is necessarily Earth-like. For example, the high latitude magnetic field concentrations that dominate the historical geomagnetic field (Jackson et al., 2000) are prominent in dynamos with large and intermediate Ekman numbers, but less prominent in dynamos at lower Ekman numbers (Takahashi et al., 2008).

Scaling laws offer some guidance for selecting the control parameters in a dynamo model. The dipole magnetic field in our model extrapolates rather well to the geodynamo, according to scaling relations derived by Christensen and Aubert (2006). In terms of the dimensionless parameters of our model, the rms dipole field for convective dynamos in the dipolar regime (Olson and Christensen, 2006) can be written

$$B_d = \gamma(PmE)^{1/2}Pr^{-1/3}(Ra - Ra_{cr})^{1/3} \quad (7)$$

where  $\gamma$  is a coefficient of proportionality and  $Ra_{cr}$  is the critical Rayleigh number for convective onset. In terms of dimensional parameters, (7) is

$$B_d(cmb) = \gamma(\rho\mu_0)^{1/2}(g_0\beta(\dot{\chi}_0 - \dot{\chi}_{cr})D^2)^{1/3} \quad (8)$$

where  $B_d(cmb)$  is the time average rms dipole field strength on the core-mantle boundary in Tesla, and  $\dot{\chi}_{cr}$  is the critical rate of light element increase for convective onset. In our dynamo model the dimensionless time average rms dipole strength is  $B_d \simeq 0.7$  and the supercritical Rayleigh number is  $Ra - Ra_{cr} \simeq 1.1 \times 10^4$ , which give  $\gamma \simeq 0.087$  in (7). For the geodynamo, we assume  $\rho = 11 \text{ Mg m}^{-3}$ ,  $g_0 = 10.7 \text{ m s}^{-2}$ ,  $\beta = 1$ , (Jones, 2007),  $\mu_0 = 4\pi \times 10^{-7} \text{ H m}^{-1}$ ,  $D = 2.258 \times 10^6 \text{ m}$ ,  $\dot{\chi}_0 - \dot{\chi}_{cr} = 2.8 \times 10^{-19} \text{ s}^{-1}$  (with  $\dot{\chi}_0 = 0.1$  this is equivalent to an inner core growth rate of approximately  $\dot{r}_{ic} \simeq 2.5 \times 10^{-11} \text{ m s}^{-1}$ ) and  $B_d(cmb) = 0.26 \text{ mT}$ . These give  $\gamma \simeq 0.089$  in (8), essentially the same as our dynamo model.

Finally, large  $E$  dynamos allow for coarse numerical grids with large time steps. This makes them particularly suitable for modeling the paleomagnetic field, where very long simulation times are needed to capture polarity chrons, reversals, and other low frequency variability, yet only the low degree part of the field is of much interest. For this same reason, large  $E$  dynamos are usually easier to interpret. Our model produces relatively simple large-scale flows and dipole-dominated magnetic fields, whereas smaller  $E$  dynamos often have a complexity that tends to obscure the dipole collapse and reversal mechanisms.

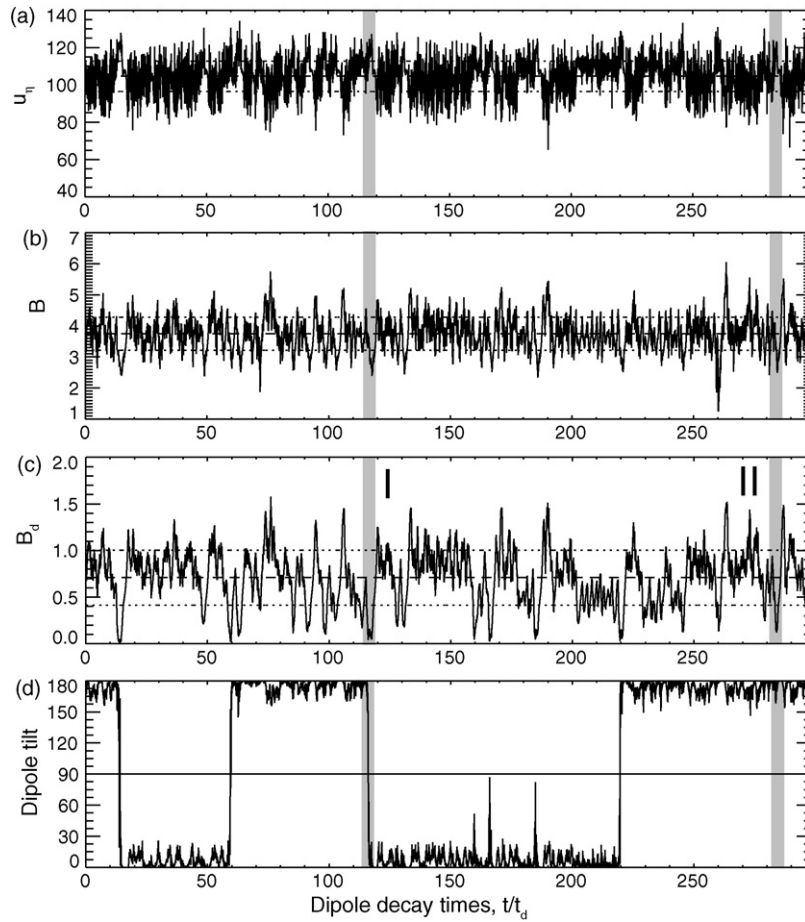
#### 5. Results

Fig. 1 shows full-length time series of the model behavior over nearly 300 dipole decay times, equivalent to about 6 Myr of paleomagnetic time. The calculation was started with a strong axial dipole field and random buoyancy (light element) perturbations. The first ten dipole diffusion times have been removed in order to minimize contributions from the initial transients. Even with the initial transients deleted, we find that a very long-duration run is necessary for this type of study. Although the control parameters and the boundary conditions are unchanged throughout the simulation, this dynamo exhibits a surprising amount of low frequency variability, so that very long time averages are required for all of its statistical properties to approach stationarity. For example, the rate of approach to zero polarity bias is extremely slow in this model. Not only are the individual constant polarity epochs in Fig. 1 long-lasting (of order 100 dipole diffusion times on average), they also show some tendency for dispersion, i.e., lengthening over the course of the simulation.

The time series of rms fluid velocity, internal magnetic field, and outer boundary dipole field strength in Fig. 1 all show continuous, large amplitude fluctuations about their respective mean values. The tilt of the dipole axis (relative to the north geographic pole) is also continuously variable, although it has a strong bias toward polar orientations. Four polarity reversals and three dipole axis excursions occur in this time interval, as well as about 15 instances when the dipole falls below 20% of its average intensity, events that qualify as dipole collapses. Overall, nearly one-half of these dipole collapses result in either dipole axis excursions or polarity reversals, with the reversals occurring during the most severe of the dipole collapses. Significantly, neither of the two brief reductions of the internal magnetic field in Fig. 1 (dynamo collapses, at times  $t/t_d = 72$  and 260) produced polarity reversals or major dipole axis excursions, and indeed the dipole remained highly axial during both of these. The velocity fluctuations have a relatively high frequency content compared to the dipole field. The rms internal magnetic field fluctuations are generally correlated with the dipole field intensity fluctuations. Comparison of low-pass filtered versions of these records reveals a strong inverse correlation between the low frequency velocity and magnetic field fluctuations. A nonmagnetic convection calculation with the identical control parameters yielded nearly constant rms velocity, demonstrating that the Lorentz force is responsible for most of the velocity variability.

The two dipole collapses analyzed in this study are highlighted in Fig. 1. The first collapse labeled I around  $t/t_d = 116$ , resulted in a R-N (reverse-to-normal) polarity change. The second collapse labeled II around  $t/t_d = 283$  began in a similar way as the reversal event I, but produced only a minor tilt displacement and failed to reverse polarity.

The large-scale magnetic field structure on the outer boundary in our model is qualitatively similar to the present-day geomagnetic field on the core-mantle boundary (Blokhman, 2002) with the axial dipole field coming primarily from two high intensity flux patches in each hemisphere located just outside the inner



**Fig. 1.** Time series of the numerical dynamo for nearly 300 dipole decay times (approximately 6 Myr of paleomagnetic time), showing dipole collapses, polarity reversals, and excursions. (a) Rms fluid velocity in magnetic Reynolds number units; (b) rms internal magnetic field intensity; (c) rms dipole magnetic field intensity on the outer boundary; (d) dipole tilt angle. Reversing and non-reversing dipole collapses analyzed in this study are labeled *I* and *II*, respectively. Mean values and standard deviations are indicated by dashed and dotted horizontal lines, respectively.

core tangent cylinder, as shown in Fig. 2. These are maintained by a pair of large-scale anticyclonic vortices in the dynamo interior. The large-scale flows come from the model’s slow rotation, rather than from mantle control, as often inferred for the geodynamo (Amit et al., 2008; Aubert et al., 2008a). One significant difference is the size of the octupole field on the outer boundary, which is larger in our model than in the present-day geomagnetic field. This is evidenced by the weak bands of low latitude reversed flux in Fig. 2, as opposed to the intense normal flux patches found at low latitudes in the geomagnetic field (Jackson, 2003).

5.1. Statistics

Statistical comparisons of our model with properties of the geomagnetic core field and the flow inferred for the core are given in Table 1. The dipolarity in Table 1 is the ratio of rms dipole intensity to rms field intensity on the outer boundary, i.e.,  $d = B_d/B_o$ . For the present-day field on the core–mantle boundary truncated at spherical harmonic degree  $l = 14$ ,  $d \approx 0.64$  (Stacey, 1992), versus  $d = 0.55 \pm 0.12$  for our model. We note that the dipolarity of the full (untruncated) core field is probably less than 0.64, and it also may have been less in the past, when the dipole was weaker. We also note that otherwise similar reversing dynamo models with smaller  $E$  and  $Pm$ , particularly those with large amounts of buoyancy produced at the outer boundary, typically have relatively small dipolarity (Aubert et al., 2008b; Takahashi et al., 2007; Rotvig, submitted for publication).

According to Takahashi et al. (2007), rotational influence in a dynamo can be quantified in terms of the ratio of equatorially symmetric to total kinetic energy, and the ratio of equatorially anti-symmetric to total magnetic energy. Table 1 shows these ratios averaged over the whole volume and just below the outer boundary for our dynamo model, and just below the core–mantle boundary for the geodynamo. Our model and the core have essentially the same magnetic field symmetry measures on the boundary, and

**Table 1**  
Time averaged flow and magnetic field statistics for the dynamo model and the core.

	Core	Model average	Collapse	Recovery
$KE^s/KE(vol)$	–	$0.93 \pm 0.05$	$0.94 \pm 0.03$	$0.99 \pm 0.0001$
$KE^s/KE(cmb)$	$0.52 \pm 0.04$	$0.93 \pm 0.06$	$0.94 \pm 0.03$	$0.99 \pm 0.0001$
$ME^a/ME(vol)$	–	$0.93 \pm 0.04$	$0.75 \pm 0.06$	$0.98 \pm 0.004$
$ME^a/ME(cmb)$	$0.75 \pm 0.02$	$0.78 \pm 0.09$	$0.79 \pm 0.06$	$0.99 \pm 0.001$
$B_r^a/B_r(cmb)$	$0.53 \pm 0.02$	$0.67 \pm 0.06$	$0.66 \pm 0.04$	$0.93 \pm 0.01$
$Ro$	$2.5 \pm 0.4 \times 10^{-6}$	$0.03 \pm 0.002$	$0.03 \pm 0.001$	$0.03 \pm 0.001$
$Ro_l$	0.09	$0.03 \pm 0.003$	$0.03 \pm 0.001$	$0.03 \pm 0.001$
$d$	0.64	$0.55 \pm 0.12$	$0.17 \pm 0.07$	$0.58 \pm 0.02$

$KE^s(cmb)$  is the kinetic energy of the equatorially symmetric ( $s$ )  $u_\theta$  and  $u_\phi$  velocities averaged at  $r = 0.9$ .  $B_r^a(cmb)$  is the equatorially asymmetric ( $a$ ) component of  $|B_r|$  averaged at  $r = 0.9$ .  $ME^a(cmb)$  is the magnetic energy of  $B_r^a$  averaged at  $r = 0.9$ . Fluid volume averaged energies (all  $r, \theta, \phi$  components included) indicated by (*vol*). The radial field and magnetic energy ratios at the core–mantle boundary are based on the field model of Jackson et al. (2000). The core flow and kinetic energy ratios are based on the model of Amit and Olson (2006).  $Ro_l$  for the core is an estimate taken from Olson and Christensen (2006). The last two columns show statistics for the collapse and recovery phases of event *I*.

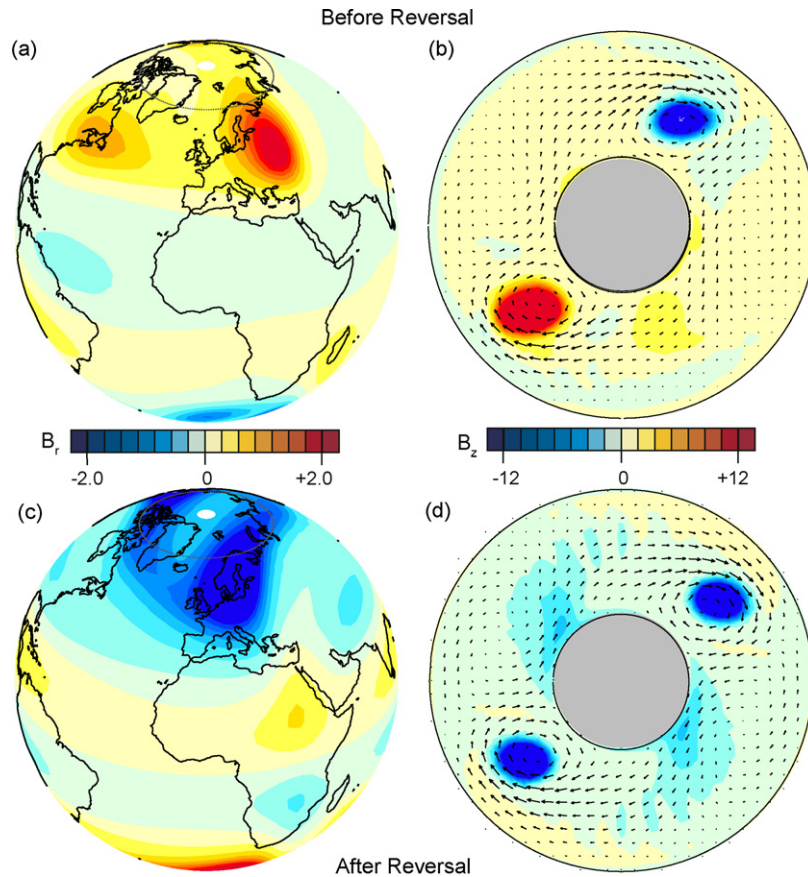


**Fig. 2.** Snapshot views before (upper) and after (lower) reversing dipole collapse *I*. (a) and (c) Contours of radial magnetic field intensity on the outer boundary (continental outlines shown for comparison purposes); (b) and (d) contours of axial magnetic field intensity in the equatorial plane with velocity arrows superimposed. Snapshot times are  $t/t_d = 115.5$  and 119, respectively.

perhaps surprisingly, our model has much higher kinetic energy symmetry than the core flow (0.93–0.52, respectively). In terms of flow structures, our model has quasi-columnar convection, a dynamical equator, and a signature of the inner core tangent cylinder, all of which have been inferred for the core flow. Viscous forces are more important in our model than in the core, and our model lacks boundary heterogeneity, which is thought to have a large effect on the symmetry of core flow (Amit and Olson, 2006). In these respects its dynamics are far from the Earth, and also far from Taylor-like dynamos found at lower  $E$  (Takahashi et al., 2005). In other respects its dynamics are more Earth-like. Although the global Rossby number  $Ro$  of our model is quite unrealistic, the local Rossby number  $Ro_l$  based on the integral length scale of the convection is within a factor of three of theoretical estimates for the geodynamo.

It is interesting to compare the proportions of equatorially symmetric kinetic energy and equatorially asymmetric magnetic energy with those of low  $E$  dynamos. Takahashi et al. (2007) report  $KE^s/KE(vol) \simeq 0.9$ ,  $ME^a/ME(vol) \simeq 0.5$ , and  $Ro_l \simeq 0.07$  for a generally less dipolar, reversing thermal convection dynamo with  $E = 2 \times 10^{-5}$ . Nishikawa and Kusano (2008) find  $KE^s/KE(vol) \simeq 0.9$  and  $ME^a/ME(vol) \simeq 0.6$  at  $E = 8 \times 10^{-4}$ . As Table 1 shows, our model is comparable to these lower  $E$  dynamos in terms of its time averaged  $KE^s/KE(vol)$ , but our time averaged  $ME^a/ME(vol)$  is significantly larger, possibly due to the large model  $Pm$ .

The statistics of time variability in the model offer additional points of comparison with paleomagnetic field statistics. The duration of individual polarity changes and dipole axis excursions in the model are comparable to the duration of geomagnetic polarity reversals and excursions inferred from the paleomagnetic record (Merrill and McFadden, 1999; Clement, 2004). The average polarity

chron length in Fig. 1 is just over 1 Myr, about twice the average polarity chron length for the whole of the sea floor record, and several times longer than the average chron length over the past 5 Ma (Constable, 2003). The frequency spectrum of the outer boundary rms dipole field  $B_d$  in Fig. 3 shows a broad, continuous distribution of frequencies that decrease approximately as  $f^{-7/3}$  in the band centered around the characteristic dipole decay frequency  $f_d$ . The general shape of the dipole frequency spectrum is similar to estimates of the geomagnetic power spectrum in this frequency range (Constable and Johnson, 2005). The histogram of axial dipole amplitudes in Fig. 3 approximates two overlapping, nearly Gaussian distributions, like the histogram of paleomagnetic field intensity (Constable and Parker, 1988). The dipole axis locations in Fig. 3 cluster within  $20^\circ$  of each pole, with no detectable longitude bias.

## 5.2. Dipole collapse with reversal

Fig. 4 shows details of the time series for dipole collapse *I*, over about 5 dipole decay times (approximately 100 kyr on Earth). This time interval was chosen to cover the events leading up to and following the dipole collapse and reversal processes. The inverse relationship between the low frequency velocity and magnetic fluctuations is evident in these time series. In the first part of the record, the high frequency variations of the outer boundary rms dipole field  $B_d$ , the rms internal field intensity  $B$ , and the rms fluid velocity  $u_\eta$  are all relatively small in amplitude, with the velocity fluctuations leading the magnetic field fluctuations by nearly one quarter cycle, the model producing more magnetic energy than is being dissipated and increasing the dipole strength. The dipole reaches its

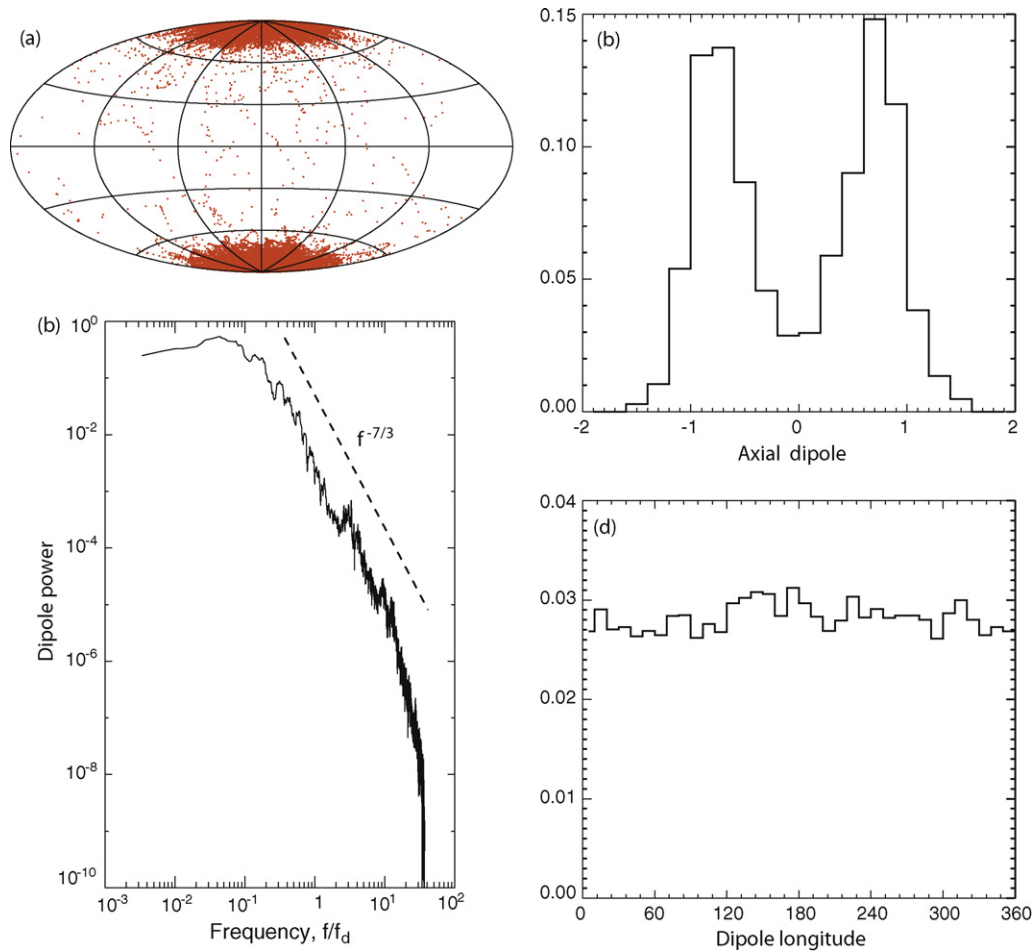


**Fig. 3.** Dynamo model statistics over 300 dipole decay times. (a) Dipole axis locations; (b) histogram of axial dipole intensity; (c) frequency spectrum of dipole fluctuations ( $f_d = 1/t_d$ ); (d) histogram of dipole longitudes.

peak intensity near  $t/t_d = 115.4$ , and about this time the velocity fluctuations begin to increase in amplitude. The internal magnetic field peaks shortly thereafter, whereupon both  $B_d$  and  $B$  decrease rapidly. The rms fluid velocity and its high frequency fluctuations both increase during the dipole collapse, but the phase relationship between the high frequency velocity and magnetic field fluctuations is irregular.

The major directional instability of the dipole axis begins around  $t/t_d = 115.7$  in Fig. 4 and includes a short episode of dipole tilt decrease. After  $t/t_d = 115.9$  the tilt increase becomes faster and more monotonic, lasting until about  $t/t_d = 116.6$ , roughly corresponding to 10 kyr on Earth. However, there are significant dipole tilt fluctuations of  $15\text{--}25^\circ$  before and after the major directional transition. The dipole remains weak until about  $t/t_d = 117.5$ , when it begins a monotonic increase back to a high value in the normal polarity state. Velocity fluctuations are quite small during this recovery phase, even smaller than during its increase prior to collapse. But as in the initial increase, these fluctuations lead the magnetic fluctuations by about a quarter cycle. Measured by the duration of weak dipole intensity, the collapse lasts nearly  $2t_d$ , about 40 kyr on Earth. Measured by time from peak dipole intensity to reversal, the collapse lasts nearly  $t_d$ , about 20 kyr on Earth. Note that the dipole intensity never vanishes during the reversal and in fact remains above  $B_d = 0.1$ , indicating that the equatorial component of the dipole is relatively strong during the polarity change. Also note that in recovery,  $B_d$  changes precede  $B$  changes, whereas the reverse applies to the collapse, indicating that dipole collapse and recovery occur via different processes. Later in this section

we provide spectral evidence that the collapse is basically a magnetic field mixing phenomenon, with energy cascading to higher wavenumber, whereas energy flows toward lower wavenumber during the regeneration.

Fig. 2 shows snapshots of the radial magnetic field structure on the outer boundary and the structure of the axial field in the equatorial plane, prior to and after the polarity change, at times  $t/t_d = 115.5$  and  $t/t_d = 119$ , respectively. The axial field is concentrated in flux ropes in the equatorial plane, located near the centers of the two prominent anticyclones. Between the equatorial plane and the outer boundary, these flux ropes are twisted, partially unravel, and are re-concentrated by fluid downwellings, producing the high latitude patches of concentrated flux patches on the outer boundary seen in Fig. 2. Prior to the reversal, the two axial flux ropes in the equatorial plane have opposing polarity, although the positive polarity rope is stronger and controls the overall dynamo polarity (see Fig. 5). Because of this polarity control, the field on the outer boundary lacks a reversed flux spot from the weaker negative flux rope in the interior. Its presence is implicit, however, in the absence of a second strong positive flux patch on the outer boundary. Dynamo regeneration is less efficient with this complex internal magnetic field structure. The velocity is highly time variable because the Lorentz force is large and variable, and the dipole is prone to fluctuate as the two competing axial flux ropes vie for control. The actual polarity reversal corresponds to the instant when the two opposing flux ropes attain equal strength. In the snapshot after the reversal, both equatorial flux ropes are negative and the boundary field has two comparably strong negative flux patches in

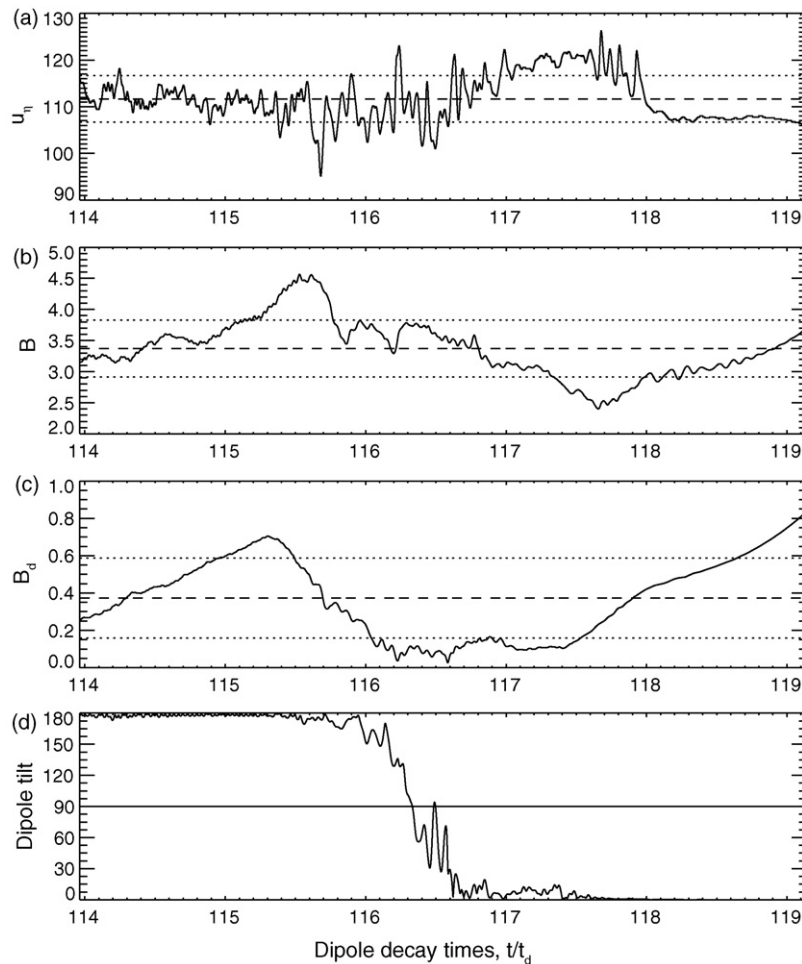


**Fig. 4.** Detailed time series of numerical dynamo model during dipole reversing collapse I. (a) Rms fluid velocity in magnetic Reynolds number units; (b) rms internal magnetic field intensity; (c) rms dipole magnetic field intensity on the outer boundary; (d) dipole tilt angle. Mean values and standard deviations are indicated by dashed and dotted horizontal lines, respectively.

the northern hemisphere. Dynamo regeneration is more efficient in this mode.

Fig. 5 shows the configuration of internal magnetic field lines during dipole collapse I. Fig. 5a shows the mixed polarity internal state at  $t/t_d = 115.5$  during the collapse phase prior to the reversal

and Fig. 5b shows the uniform internal polarity state at  $t/t_d = 118.8$  during the recovery phase following the reversal. The field lines are colored according to the sign of their axial component in the equatorial plane, in order to emphasize the structure of the two main flux ropes.

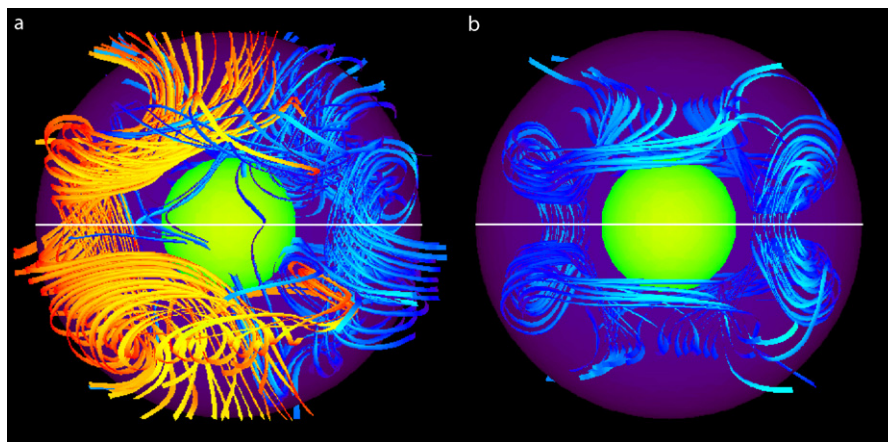


**Fig. 5.** Internal dynamo magnetic field lines during and after reversing collapse I, viewed from the equatorial plane. (a) Mixed polarity state at time  $t/t_d = 115.5$  during collapse phase; (b) uniform polarity state at time  $t/t_d = 118.8$  during recovery phase. Magnetic field lines are colored according to the sign of their axial component in the equatorial plane; red-yellow = axial positive, blue-purple = axial negative. Outer boundary shaded in purple, inner boundary shaded in green, equator shown as white line. Images (a) and (b) correspond to Figs. 16 and 17, respectively.

Prior to the reversal the positive flux rope is slightly stronger and dominates the dipole polarity, although the negative rope is sufficiently strong that some of its field lines cut the outer boundary, forming the reversed flux patches that are analyzed in Figs. 7 and 16. Other field lines reconnect directly from the weaker to the stronger flux rope entirely within the core; these are indicated by the few reverse color lines entering or leaving each of the flux ropes (Fig. 5a). Compared with the highly symmetric field structure in Fig. 5b corresponding to the recovery phase, the more complex structure of the field in Fig. 5a is indicative of a higher level of time variability during the collapse phase. Note that the two flux ropes in Fig. 5 are bent by the retrograde motion of the anticyclonic vortices, so that their intersections with the outer boundary lie to the east of their positions in the equatorial plane. Overall, the mixed polarity state is far more common than the uniform polarity state, the latter only existing during rapid dipole increases. The reversed flux rope that caused this reversal was spawned in a previous collapse event, long before the one depicted here.

Fig. 6 is a streak diagram showing the evolution of the axial vorticity and magnetic flux in the equatorial plane as a function of time and longitude during collapse I. The upper panel shows contours of the integrated

vorticity flux

$$S_{\omega}(\phi, t) = \int_{r_i}^{r_o} \omega_z(z=0)r \, dr \tag{9}$$

and the lower panel shows contours of the integrated magnetic flux

$$S_B(\phi, t) = \int_{r_i}^{r_o} B_z(z=0)r \, dr \tag{10}$$

The streaks in Fig. 6 correspond to the motion of the concentrated vortices and magnetic flux ropes in the equatorial plane and the negative slope of the streaks is a consequence of their westward (retrograde) drift. The background color of the  $S_B$  panel indicates the prevailing magnetic polarity, which transitions from reverse ( $B_z > 0$ ) to normal ( $B_z < 0$ ) over time. The vorticity streaks are mostly negative, reflecting the dominance of the anticyclones, whereas the magnetic streaks are positive and negative before the reversal, and change to only negative well after the reversal has taken place. Note that the vorticity streaks appear less continuous in the middle of Fig. 6, an expression of the increased flow variability and decreased structural continuity during the collapse.

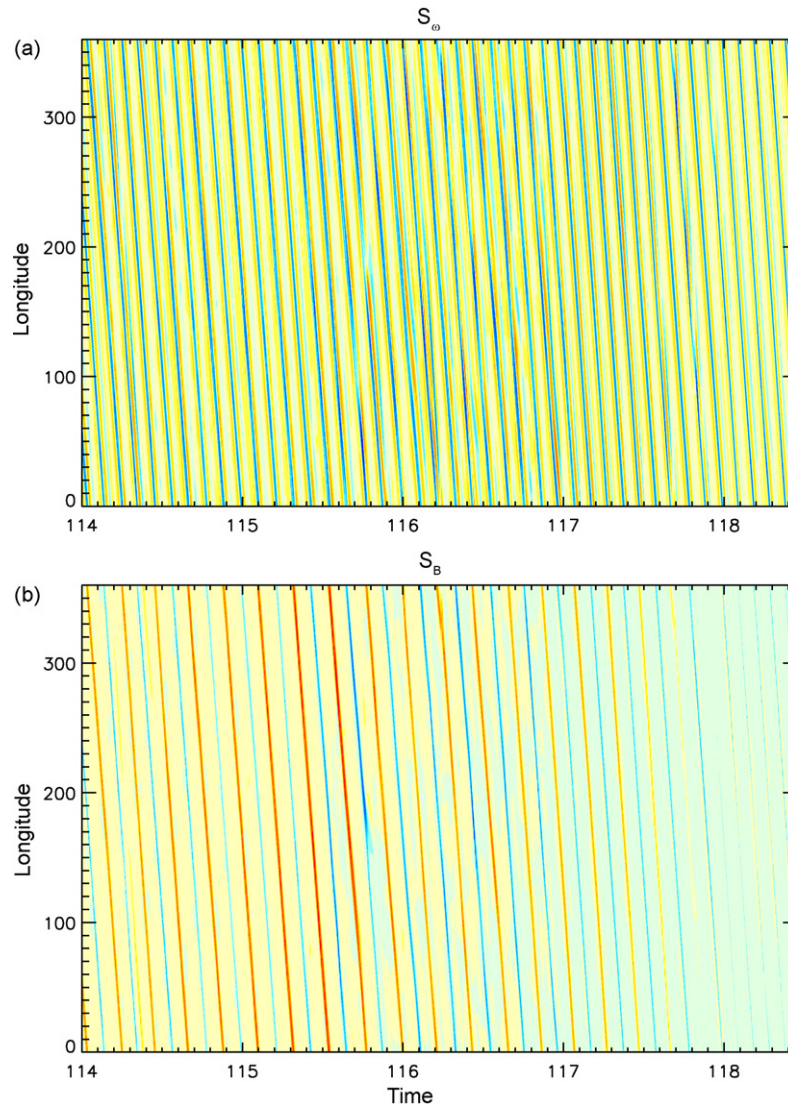
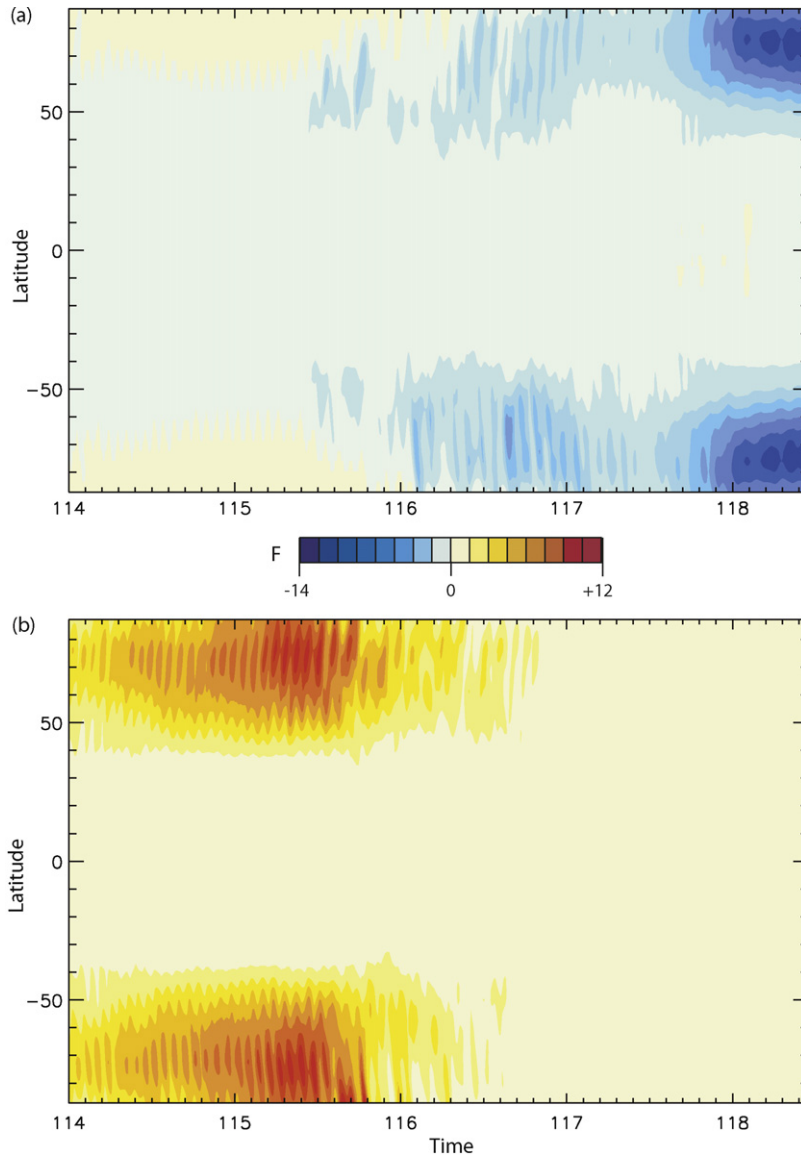


Fig. 6. Streak diagrams showing the radially integrated axial vorticity and axial magnetic field in the equatorial plane as a function of time and longitude during reversing collapse I. (a) Axial vorticity  $S_{\omega}$ ; (b) axial magnetic field  $S_B$ . Red and blue contours denote positive and negative values, respectively.



**Fig. 7.** Butterfly diagrams showing the contributions from radial magnetic field on the outer boundary to the axial dipole as a function of latitude and time during collapse I. (a) Contours of the negative part of  $F$ ; (b) contours of the positive part of  $F$ .

Fig. 7 shows time-latitude contour plots of the quantity

$$F(\theta, t) = \int_0^{2\pi} \rho_z d\phi \quad (11)$$

during collapse I, where  $\rho_z = B_r(r = r_o) \cos \theta$  is the dimensionless axial dipole moment density on the outer boundary. The contributions to  $F$  from locally negative and locally positive  $\rho_z$  are contoured separately; hereafter we refer to these as the negative and positive parts of  $F$ , respectively. The patterns in Fig. 7, which are reminiscent of the butterfly diagrams invented by Maunder (1913) to interpret the cycles of the solar dynamo (Ossendrijver, 2003; Ternullo, 2007), reveal the appearance and disappearance of the normal and reversed boundary flux, highlighting their separate effects on the evolution of the axial dipole field.

The butterfly wings of  $F$  in Fig. 7 occur in the form of mid- and high-latitude sets in each hemisphere, and are separated by a broad low latitude band where the boundary field contributes little to the axial dipole. Individual wings trace the latitudinal evolution of one or more patches of concentrated magnetic flux on the outer boundary induced by velocity fluctuations and magnetic upwellings. The

slopes of the wings indicate that magnetic flux concentrations first emerge at mid-latitudes and then migrate poleward in each hemisphere before disappearing. Narrow articulated wing structures reflect the increased high frequency dynamo variability and general poleward migration of the field during dipole collapse. These structures are produced by pulsations in the strength of the flux ropes shown in Fig. 5.

The more diffuse wing structures during dipole recovery reflect the reduced dynamo variability and lack of poleward migration. There is an early outbreak of reversed flux wings just after the dipole moment peaks at  $t/t_d = 115.5$ , signaling the onset of the dipole collapse. This precursor is followed by a minimum in activity, followed by the main outbreak of reversed flux, which emerges around  $t/t_d = 116.1$ , well after the collapse is underway but simultaneous with the major tilt increase, and continues through the reversal. The relatively small difference in scale used for the negative and positive contours in Fig. 7 indicates that the reversed flux precursors are relatively strong in this case. During the dipole recovery phase the dominant polarity wings display little or no poleward drift, either because the flux patches are stationary or are being continuously regenerated.

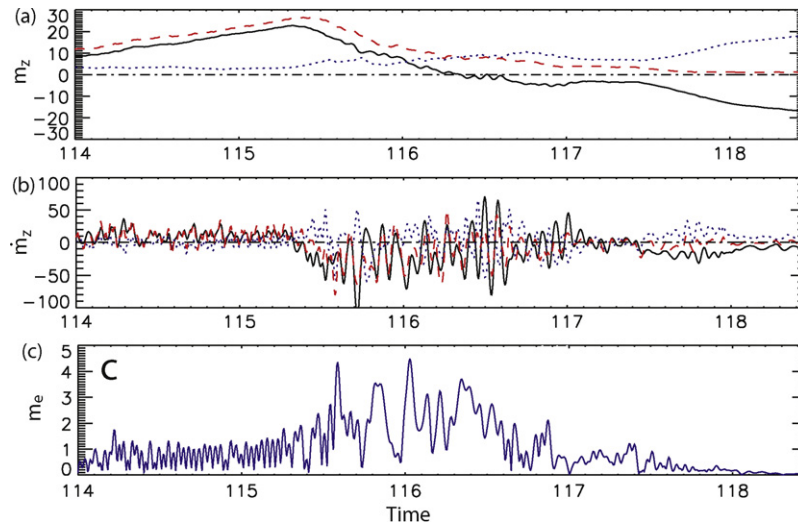


**Fig. 8.** Time series of dimensionless axial and equatorial dipole moments during reversing collapse I. (a) Positive part (dashed), negative part (dotted), and total (solid)  $m_z$  from radial field on the outer boundary; (b) positive part (dashed), negative part (dotted), and total (solid)  $\dot{m}_z$  from radial field change on the outer boundary; (c) equatorial dipole moment  $m_e$ .

Fig. 8 shows the positive and negative contributions to the dimensionless axial dipole moment  $m_z(t)$  and its time derivative  $\dot{m}_z(t)$ , obtained by separately integrating the positive and negative parts of  $\rho_z$  over the outer boundary. The dimensionless equatorial dipole moment  $m_e(t)$  is also shown for comparison. During dipole

growth and collapse phases, most of the variation in  $m_z$  is due to changes in the prevailing field on the outer boundary, rather than the competing field. As seen in previous figures, the primary difference between collapse and growth is the amount of high frequency variability, which is large during collapse and small during growth

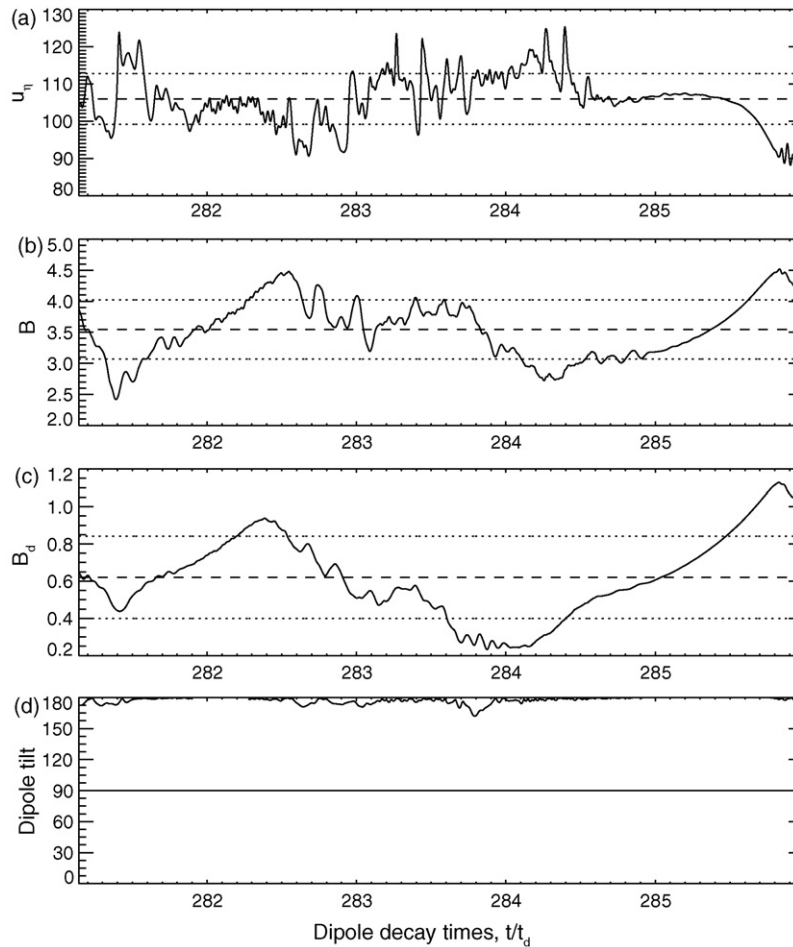


**Fig. 9.** Detailed time series of numerical dynamo model during dipole non-reversing collapse II. (a) Rms fluid velocity in magnetic Reynolds number units; (b) rms internal magnetic field intensity; (c) rms dipole magnetic field intensity on the outer boundary; (d) dipole tilt angle. Mean values and standard deviations are indicated by dashed and dotted horizontal lines, respectively.

phases. The increased variability during the dipole collapse is particularly evident in  $m_e$ . Growth of the equatorial dipole at the height of the dipole collapse enhances the probability for polarity reversal by rotating the dipole axis toward the equator.

In addition to increased high frequency variability, the dipole collapse involves a change in the symmetry of the flow with respect to the equatorial plane. Nishikawa and Kusano (2008) report decreases in the  $KE^S/KE(vol)$  and  $ME^d/ME(vol)$  ratios during dipole collapse events. As seen in Table 1, these ratios are both smaller during the collapse than the recovery phase in our model. We note that the primary difference between the collapse and recovery flows is a large increase in the asymmetric part, by a factor of  $\sim 100$ , during the collapse.

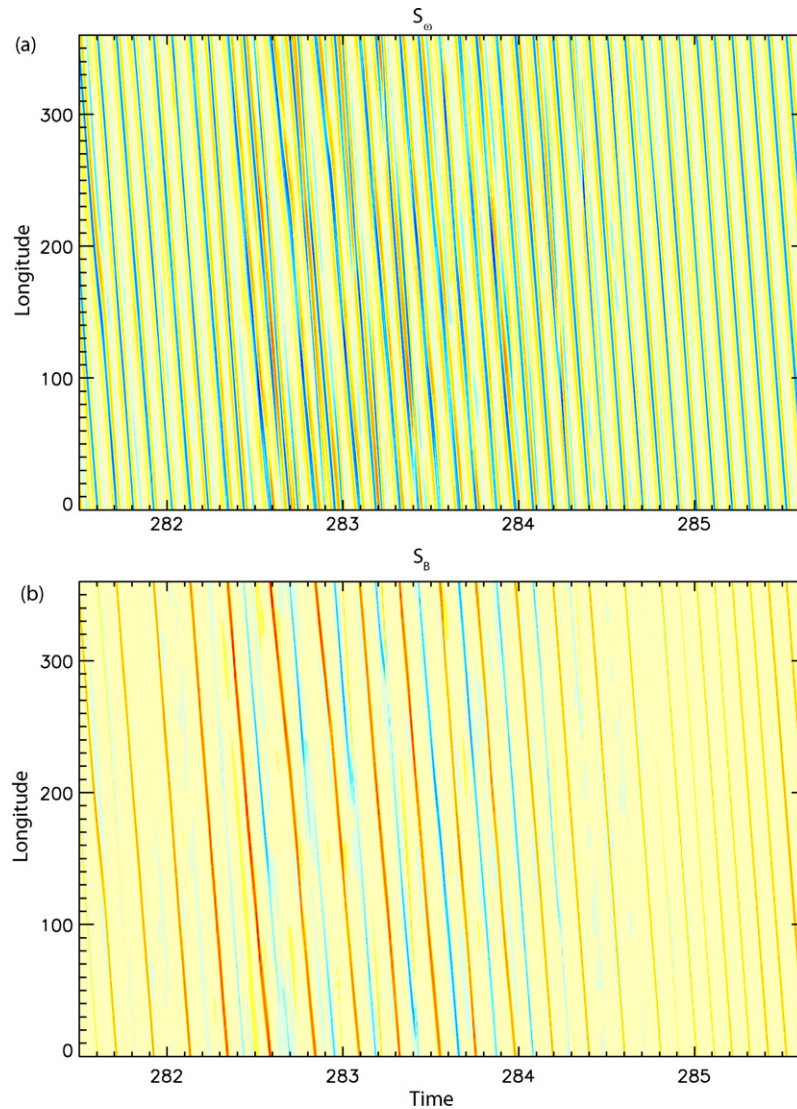
### 5.3. Dipole collapse without reversal

Fig. 9 shows time series details of dipole collapse II, Fig. 10 shows the equatorial streak patterns, Fig. 11 shows the butterfly pattern during this time, and Fig. 12 shows the evolution of the axial and equatorial parts of the dipole. Most of the processes identified in collapse I are also present in collapse II. In particular, the high frequency variability is large during collapse and small during recovery phases, a negative magnetic flux rope appears in the

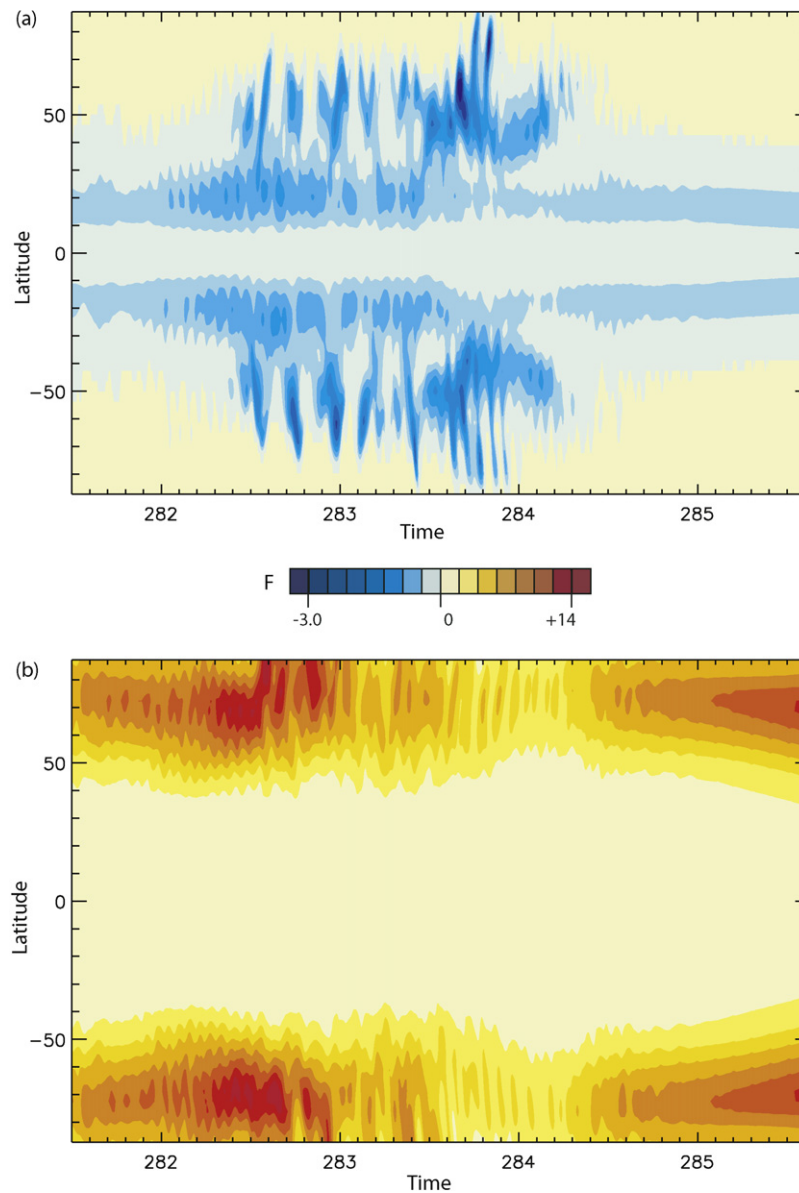
equatorial plane, there is a precursory outbreak of reversed flux butterfly wings on the outer boundary at  $t = 282.5t_d$ , prior to dipole collapse, and the equatorial dipole grows during the collapse phase. The dipole collapse in this case began with the dipole field being somewhat stronger than in the previous case. Collapse II did not produce a polarity reversal, and in fact produced only a relatively minor ( $\sim 20^\circ$ ) dipole tilt.

Fig. 9 covers portions of three dipole reductions, including a collapse near  $t/t_d = 284$  in which the dipole moment decreases to about 10% of its previous peak value in just over one dipole decay time. It also includes two complete dipole recoveries. The short-term variability is low during both recoveries and high during all three decreases. The transition between high and low short-term variability is particularly evident in the velocity at  $t/t_d = 282.4, 284.5,$  and  $285.8$ . The first and last of these times correspond to dipole maxima, and the second occurs during the sustained recovery phase after the collapse. These associations provide additional evidence that short-term variability in the convection is closely associated with dipole collapse.

The dipole collapse is marked by the transient appearance of a negative magnetic flux rope in the equatorial plane, as seen in Fig. 10. This negative flux rope appears when the flow becomes variable, as evidenced by the discontinuous vorticity streaks about



**Fig. 10.** Streak diagrams showing the radially integrated axial vorticity and axial magnetic field in the equatorial plane as a function of time and longitude during non-reversing dipole collapse II. (a) Axial vorticity  $S_\omega$ ; (b) axial magnetic field  $S_\beta$ . Red and blue contours denote positive and negative values, respectively.



**Fig. 11.** Butterfly diagrams showing the contributions from radial magnetic field on the outer boundary to the axial dipole as a function of latitude and time during collapse II. (a) Contours of the negative part of  $F$ ; (b) contours of the positive part of  $F$ .

that time. The ephemeral nature of this negative flux rope is the primary reason that collapse II did not produce a polarity reversal. Once the negative flux rope fades, the flow loses its variability and the dipole recovers.

The same sequence of events seen in the equatorial flux ropes is also evident on the outer boundary. As shown in Fig. 11, the negative butterfly wings appear at middle latitudes on the outer boundary at the same time that the increased convective variability and the negative flux rope appears in the equatorial plane. Likewise, negative butterfly wings disappear from the outer boundary when the negative flux rope disappears from the equatorial plane. The poleward migration of flux is evident during the dipole collapse but less regular compared to the reversing case in Fig. 7. Only a few of the negative butterfly wings propagate to polar latitudes in this case, corresponding to the time when the negative flux rope in Fig. 10 is strongest. However, as the negative flux rope loses its strength the negative wings on the outer boundary also weaken, the positive wings emerge, and the dominant polarity is recovered. The relationships between convective variability and the components of the dipole moment and dipole tilt variations seen during collapse

I are clearly evident during event II, as shown in Fig. 12, although with smaller amplitudes.

Note the large difference in scale used for the negative and positive contours in Fig. 11, which indicates that the reversed flux precursors are relatively weak in this case. In case I, the amplitude of the contributions to  $F$  from negative  $\rho_z$  prior to the reversal amount to about 40% of the amplitude of the contributions to  $F$  from positive  $\rho_z$ . In contrast, this ratio is only 20% in case II. This ratio may provide a criterion for distinguishing reversing from non-reversing dipole collapses. According to our results, its critical value is within the range of 20–40%.

#### 5.4. Spectral evolution of the velocity and magnetic fields

We have shown that an outbreak of reversed magnetic flux appears on the outer boundary as a transient precursor to dipole collapse, that the dynamo has more high frequency variability during dipole collapse than during dipole recovery. In addition to increased time variability, there is some decrease in equatorial symmetry of the convection associated with the dipole collapse.

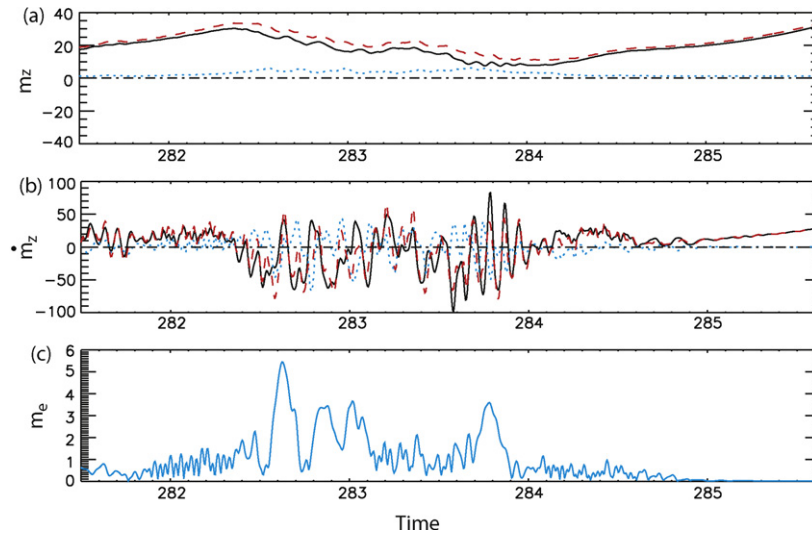


**Fig. 12.** Time series of dimensionless axial and equatorial dipole moments during collapse II. (a) Positive part (dashed), negative part (dotted), and total (solid)  $m_z$  from radial field on the outer boundary; (b) positive part (dashed), negative part (dotted), and total (solid)  $\dot{m}_z$  from radial field change on the outer boundary; (c) equatorial dipole moment  $m_e$ .

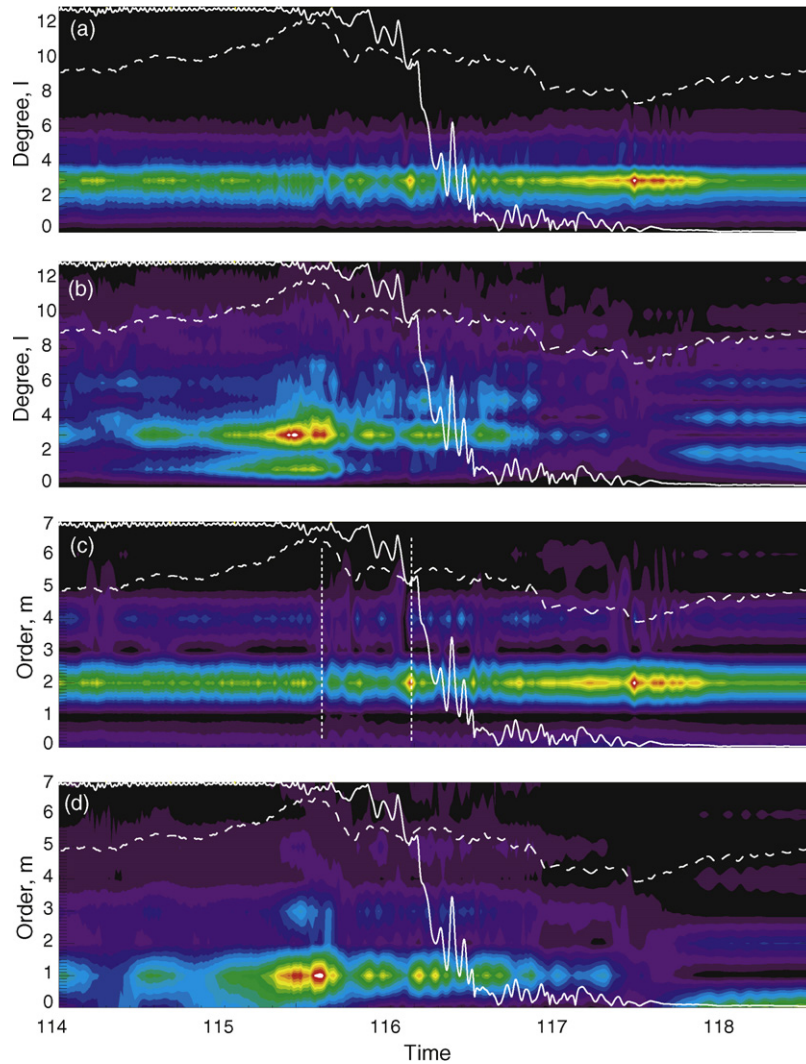


**Fig. 13.** Power spectra versus time during collapse I. (a) Kinetic energy versus harmonic degree  $l$ ; (b) internal magnetic energy versus harmonic degree; (c) kinetic energy versus order  $m$ ; (d) internal magnetic energy versus order  $m$ . Spectra are normalized by their respective maximum values (white). Internal field rms intensity (dashed) and dipole tilt (solid) time series are superimposed for reference.

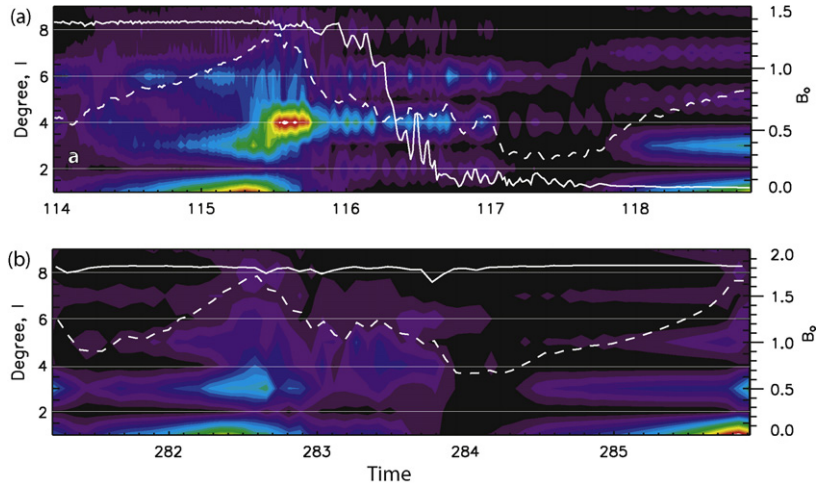


**Fig. 14.** Magnetic field power spectra on the dynamo model outer boundary versus time during dipole collapses *I* (a) and *II* (b). Contours show power at spherical harmonic degrees *l* (integer values only). Internal field rms intensity (dashed, right scale) and dipole tilt (solid) time series are superimposed for reference.

Major structural changes are not evident in the streak diagrams of equatorial vorticity, so we investigate the spectral content of the flow away from the equatorial plane. Fig. 13 shows power spectra of the internal kinetic and magnetic energies versus time during collapse *I*, with the time series of rms internal field intensity and dipole tilt superimposed for reference. The inverse correlation between low frequency magnetic and kinetic energy fluctuations are clearly evident in these spectra. The differences in the polarity of the magnetic ropes before and after reversal is also clearly evident in the transition from dominant azimuthal  $m = 1$  mode to dominant azimuthal  $m = 0$  mode in the energy content of the internal magnetic field. Changes in the shape of the kinetic energy spectra appear to be minor by comparison. Indeed we find no evidence for major or sustained structural changes in the flow during either collapse *I* or *II*. However, there are several short-lived fluctuations in total kinetic energy that coincide with the major changes in magnetic field behavior. Two such brief fluctuations are marked by vertical dashed lines in Fig. 13. These kinetic energy spikes correspond to surges in the convective flow, while the kinetic energy holes correspond to time increments between the decay of a large anti-cyclonic vortex and the formation of its replacement. Additional kinetic energy spikes occur elsewhere in the record, however. It is possible (although not conclusively demonstrated here) that these short-lived events, particularly the kinetic spikes, signal the increased high frequency variability which precipitates the longer-term changes in the magnetic field structure.

Unlike the convective velocity, the magnetic field spectra show fundamental differences between dipole generation and collapse phases. Fig. 14 shows the evolution of magnetic field power spectra on the dynamo model outer boundary over time during events *I* and *II*. The contours show power at spherical harmonic degrees *l* (integer values only), the white lines show  $B_o$ , the rms magnetic field on the outer boundary, and the yellow lines show the dipole tilt angle. The comparison between  $B_o$  and the  $l = 1$  harmonic demonstrates that the rms field intensity on the outer boundary peaks well after the dipole collapse is underway, especially in the reversing case *I*. In both cases there is a forward cascade of magnetic energy during the collapse event, as peak energy moves from the dipole  $l = 1$  term to the octupole  $l = 3$  term to the hexadecapole  $l = 4$  term, and finally to the  $l = 6$  term at the time of the directional instability. Evidently the flow variability associated with the dipole collapse preferentially strengthens even harmonics in the outer boundary field. This effect is stronger in case *I* where the dominant harmonic is  $l = 4$  during most of the collapse and reversal. For both cases the spectrum of the boundary field during dipole recovery includes odd harmonics,

which grow in phase. No cascade of magnetic energy is evident in the recovery, and the rms field intensity  $B_o$  increases in step with the rms dipole intensity  $B_d$  and all the other odd harmonics of the boundary field.

### 5.5. Scatter diagrams

Fig. 15 shows scatter plots of the dipole intensity  $B_d$  versus its time derivative  $\dot{B}_d$ , and also  $B_d$  versus the rms fluid velocity  $u_\eta$ . Here we have divided the record into two bins, one consisting of data within approximately one dipole decay time of a polarity reversal, which we refer to as unstable polarity times, the other bin consisting of the rest of the data, which we refer to as stable polarity times.

The scatter envelopes for  $B_d$  versus  $\dot{B}_d$  during stable and unstable polarity times approximate inverted Gaussians, with zero means and approximately the same width in the two cases. As expected, dipole collapses leading to polarity change reach lower dipole field intensity than collapses during stable polarity times. This is perhaps intuitive, but the difference between the two minima is nevertheless significant, since the dipole intensity never actually reaches zero at any time in this calculation, including during the four reversals. The difference between the minimum  $B_d$  during stable versus unstable polarity times indicates a threshold,  $B_d \approx 0.03$ , below which the collapse results in a reversal.

In addition, there is a well-defined saturation (maximum) dipole intensity evident in Fig. 15, both for the reversing as well as the stable polarity times. However, the saturation level for the dipole field during reversing times is less than the saturation level during stable polarity times, by almost 30%. Differences in the internal magnetic field structure during stable versus unstable polarity times suggest a possible explanation for this dipole saturation discrepancy. The highest dipole moments occur when both of the axial flux ropes have the same sign, there is little or no reversed magnetic field in the dynamo interior, and there is no high latitude reversed flux on the core–mantle boundary, the configuration illustrated in Fig. 5b. Some of the non-reversing collapses in this study start from a magnetic field in this strong dipole configuration, in which case the dipole collapse involves the formation of a new reversed flux rope. These events do not produce reversals in our model, possibly because the initial dipole is too strong. The more common configuration has one magnetic flux rope already reversed with respect to the dominant field, as illustrated in Fig. 5a, and a correspondingly weaker dipole field than configuration Fig. 5b. All of the four reversing collapses in this study begin with average or less than

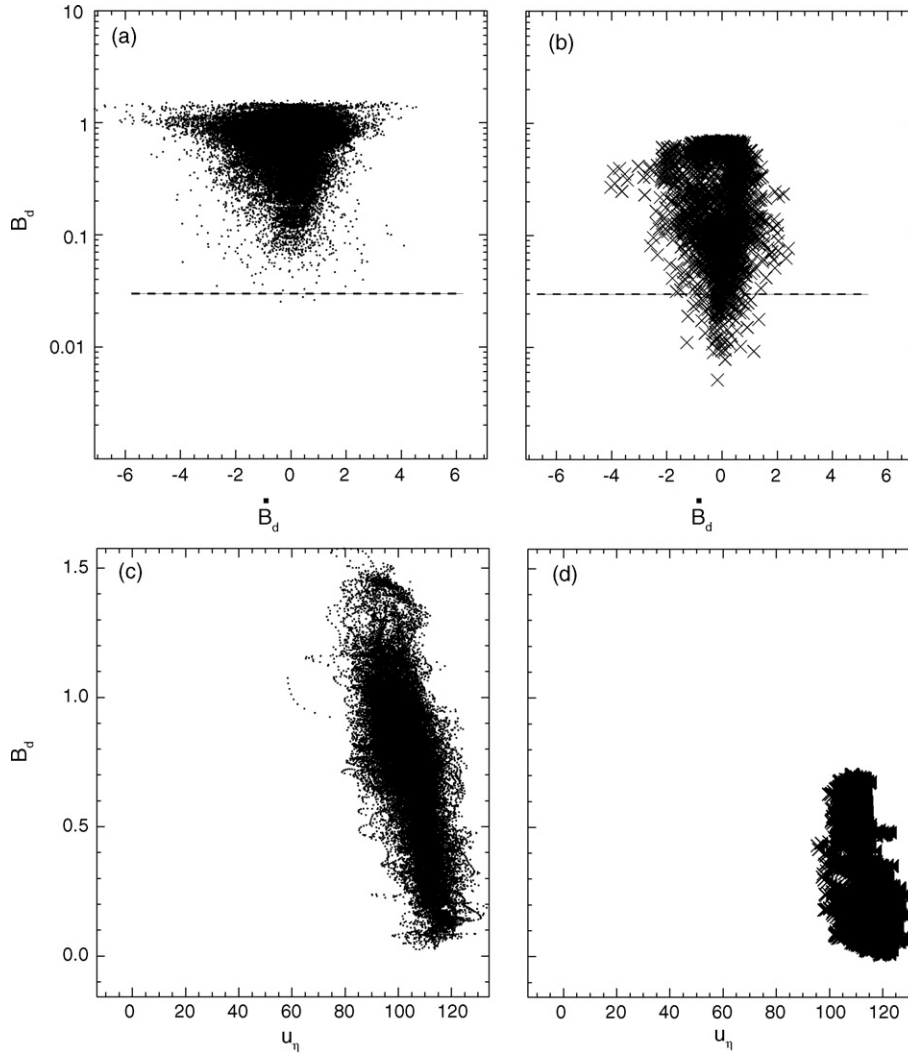


**Fig. 15.** Scatter plots of dipole field intensity and fluid velocity during stable polarity times and reversals. Left column (a, c): stable polarity times; right column (b, d): unstable polarity times within  $\pm 1t_d$  of a reversal. Top row: (a, b) dipole intensity versus its time derivative. Dashed line indicates approximate threshold separating non-reversing from reversing collapses. Bottom row (c, d): dipole intensity versus fluid velocity.

average dipole strengths. This suggests that collapse events leading to polarity reversals begin with a relatively weak dipole field, compared to non-reversing collapses, so that dipole reduction has a greater effect in one case than the other. Finally, Fig. 15 shows the general inverse relationship between velocity and dipole field intensity. The scatter in velocity under weak field conditions is somewhat larger during unstable polarity times than it is during stable polarity times, consistent with higher levels of convective variability during reversals compared with non-reversing dipole collapses.

### 5.6. Dipole change mechanisms

We can quantify the various contributions to magnetic dipole moment changes in terms of advective and diffusive magnetic induction processes. Following Moffatt (1978), axial dipole moment changes can be partitioned among three kinematic mechanisms operating just below the dynamo outer boundary. These can be written in dimensionless form as the following integral:

$$\dot{m}_z = \frac{3}{2} \int (A_z + D_{rz} + D_{tz}) r^2 \sin \theta \, d\theta \, d\phi \quad (12)$$

The contributions to  $\dot{m}_z$  by meridional advection  $A_z$ , radial diffusion  $D_{rz}$  and meridional diffusion  $D_{tz}$  are given individually by

$$A_z = -u_\theta \sin \theta B_r \quad (13)$$

$$D_{rz} = -\frac{\sin \theta}{rPm} \frac{\partial}{\partial r} (rB_\theta) \quad (14)$$

$$D_{tz} = \frac{\sin \theta}{rPm} \frac{\partial B_r}{\partial \theta} \quad (15)$$

As found previously by Olson and Amit (2006), the contribution of meridional diffusion to  $\dot{m}_z$  is typically an order of magnitude smaller than that of meridional advection and radial diffusion. We therefore focus here on the contributions of the two latter mechanisms.

Fig. 16 shows images just below the outer boundary at the beginning of the dipole collapse of case 1. At this stage, the magnetic field is still axially dipolar with a relatively small tilt, but the dipole collapse rate is fast. Three intense positive field patches are seen centered near the edge of the tangent cylinder (the polarity at this snapshot is reversed, i.e. positive in the northern hemisphere), contributing to the axial-dipolarity of the field (Fig. 16a). However, intense negative flux patches appear at mid- and high-latitudes, although these probably originate as diffusive structures at lower latitudes and are advected and concentrated by the meridional flow.

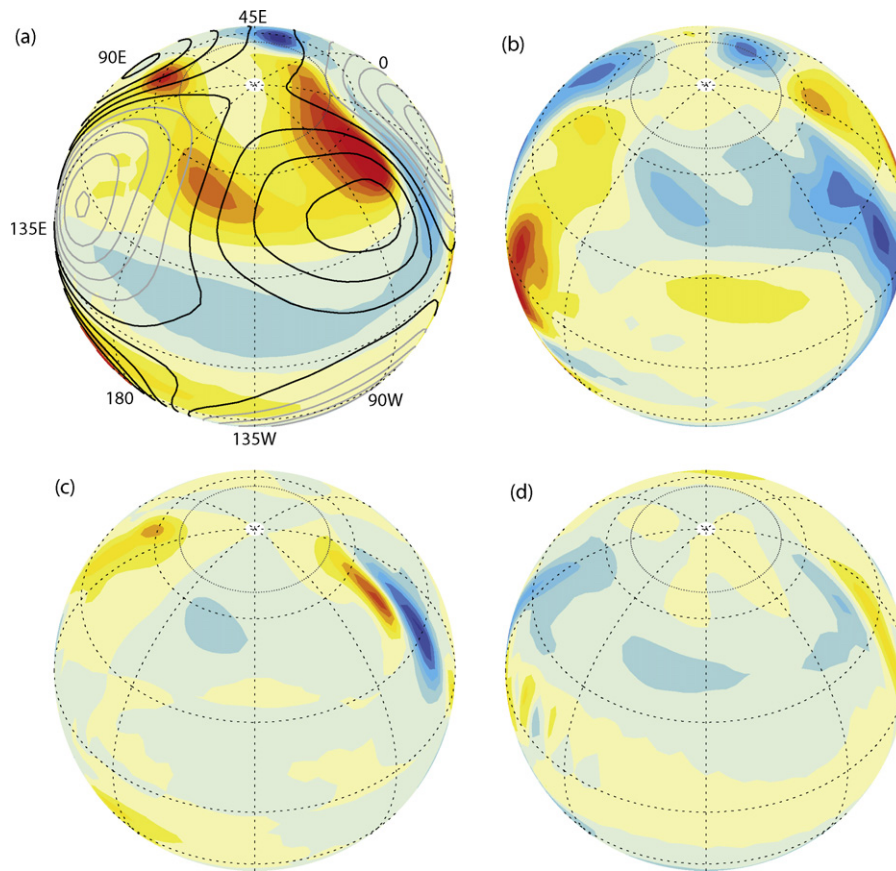


**Fig. 16.** Dipole change mechanisms during collapse phase at time  $t/t_d = 115.5$ . (a) Radial magnetic field with streamlines superimposed, black/grey denoting anticlockwise/clockwise circulation, respectively; (b) radial velocity; (c) contributions to  $\dot{m}_z$  by meridional advection  $A_z$ , and (d) by radial diffusion  $D_{rz}$ . The radial diffusion term is enhanced by a factor of three with respect to the meridional advection term. All images are constructed at the top of the free stream. Longitudes in a are shown for reference, and are the same at all images.

The convection is organized in large-scale convective columns with cyclones/anti-cyclones around descending/ascending flow (Figs. 16 a and b). Northward flow at longitude  $50^\circ\text{W}$  advects a negative flux patch and part of a positive flux patch poleward, producing a pair of advective  $m_z$  sink and source patches (Fig. 16c), with the sink being stronger. The rest of that positive flux patch is advected westward without affecting the axial dipole. Another sink appears at longitude  $160^\circ\text{W}$  where positive flux is advected equatorward, and another source appears at longitude  $120^\circ\text{E}$  where positive flux is advected poleward. Overall, advective sinks and sources due to equatorward and poleward motion of the prevailing polarity magnetic flux are balanced, whereas advective sinks due to poleward migration of opposite polarity patches contribute to the dipole collapse. Radial diffusion contributions to  $\dot{m}_z$  are generally weaker with a balanced distribution of sinks and sources.

Fig. 17 shows the same quantities at the recovery phase when the polarity is normal (negative in the northern hemisphere) and the dipole is intensifying. No significant positive magnetic flux appears in the northern hemisphere, and the magnetic field is dominated by two negative high latitude flux patches (Fig. 17a). These two structures are advected poleward, resulting in two advective axial dipole sources (Fig. 17c) that strengthen the dipole. No significant advective sinks are observed. As in the dipole collapse phase, radial diffusion contributions are weaker and nearly balanced.

Comparison of Figs. 16 and 17 shows several asymmetries between the dipole collapse and recovery phases in terms of the magnetic field structures and the source terms for the axial dipole. First, opposite-sign flux at high latitudes contribute to the dipole collapse by poleward migration, whereas the dipole recovery is attributed mostly to poleward motion of prevailing-sign flux. Sec-

ond, both advective sources and sinks are present during dipole collapse (with larger contribution from sinks), whereas dipole recovery is dominated by advective sources. Finally, local advective sinks and sources are more intense in the dipole collapse than in the dipole recovery, with the latter phase characterized by less self-cancellation. In both cases radial diffusion is less intense than meridional advection in changing  $m_z$ . However, these asymmetries are more due to differences in the internal magnetic field structure and the magnitude of the convection, rather than gross changes in the structure of the convection. Comparison of the radial velocity patterns in Figs. 16 and 17 indicates there is relatively little difference in the large-scale convective structure between these two snapshots.

## 6. Comparison with geomagnetic secular variation

Fig. 18 shows butterfly plots for the axial dipole component of the geomagnetic field on the core–mantle boundary during 1840–1990, obtained from (11) applied to the historical core field model of Jackson et al. (2000). The panel with positive values corresponds to reversed polarity magnetic field as defined by geomagnetic convention, and the panel with negative contours corresponds to the prevailing normal polarity magnetic field. Although the 150 year ( $\approx 0.01t_d$ ) time interval evidently spans much less than one full cycle of core field variation, Fig. 18 nonetheless provides qualitative evidence that the evolution of the reverse and normal magnetic field on the core–mantle boundary bears some similarity with the butterfly wings seen in Figs. 7 and 11. In particular, the roughly coincidental onset and poleward migration of the reversed polarity fields in both hemispheres, and their

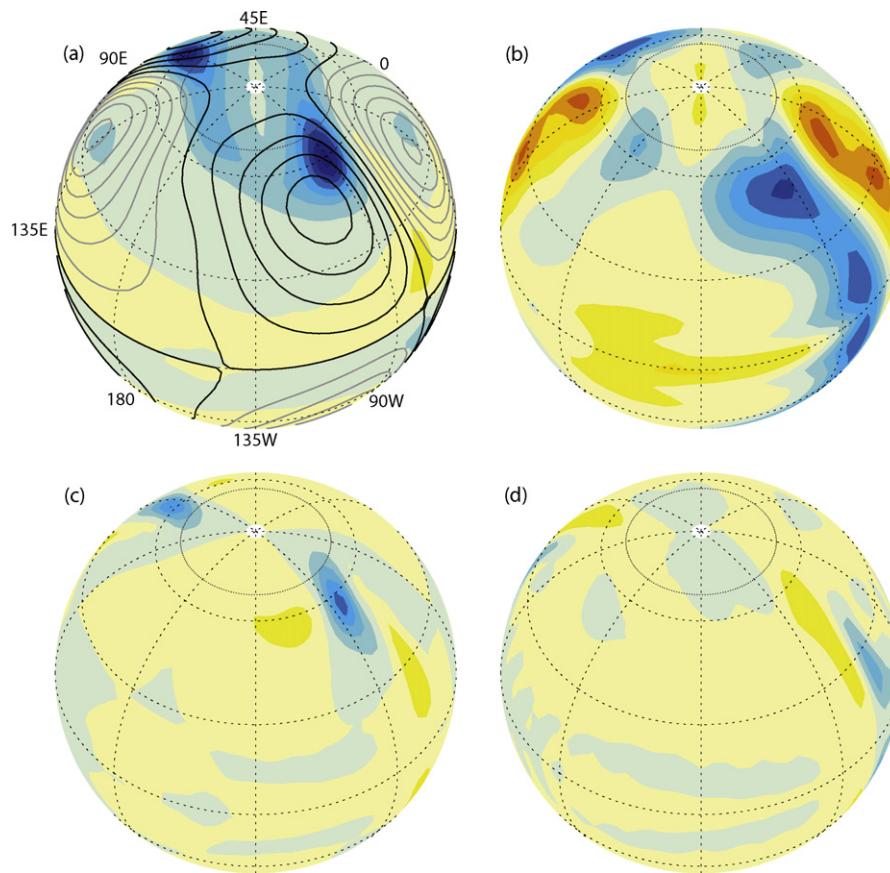


**Fig. 17.** Same as Fig. 16 during dipole recovery at time  $t/t_d = 118.8$ . All corresponding fields have the same contour intervals as in Fig. 16.

strengthening relative to the weakening contribution from normal polarity field in the southern hemisphere, are suggestive of the early stage behavior of dipole collapses in the dynamo model. One important difference is that the wing latitudes are not symmetric in the core field as they are in the dynamo model. As Fig. 18 shows, the reversed polarity wing is poleward of the normal polarity field in the northern hemisphere, but not in the southern hemisphere. In addition, the geomagnetic field pattern is generally less symmetric than the dynamo models, with the southern hemisphere contributions (positive and negative) being substantially larger compared to those in the north, as found previously by Olson

and Amit (2006). Another difference is that the prevailing normal polarity field does not show poleward propagation.

This asymmetry may be important in the future behavior of the geomagnetic field. We have already noted that one observable difference between dynamo model collapses *I* and *II* at the onset of collapse is the latitude extent of the reversed field wings, with the wings preceding reversing collapse *I* reaching higher latitudes than the wings that precede non-reversing collapse *II*. The reversed polarity field in the north polar region has the general character of a butterfly wing in the reversing dynamo collapse *I*. The southern reversed polarity wing has migrated closer to the south

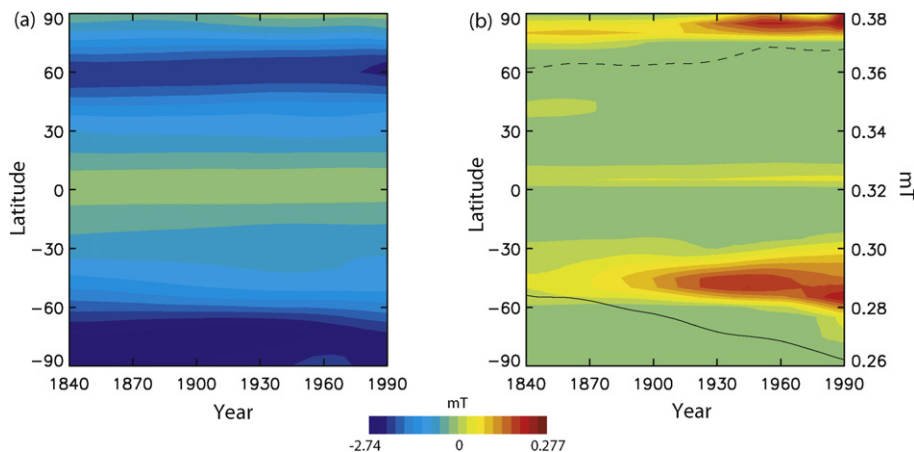


**Fig. 18.** Butterfly diagrams showing the contributions from radial geomagnetic field on the core–mantle boundary to the axial geomagnetic dipole as a function of latitude and time for 1840–1990, from the core field model *gufm1* of Jackson et al. (2000). (a) Contours of the negative part of  $F$ ; (b) contours of the positive part of  $F$ , both in mT. Superimposed are the time-series of the rms field expanded to degree and order 8 (dashed) and the rms dipole field (solid) on the core–mantle boundary.

pole by more than  $10^\circ$  of latitude since 1960 while the southern normal polarity wing has migrated somewhat equatorward, kinematic effects previously identified by Gubbins (1987) from maps of reversed flux. Assuming these trends continue, the southern wings could become more like the smaller wing structures in the northern hemisphere. If this happens, the core field pattern would then look more like the early stage of model event *I* than event *II*.

At the present time, however, the amplitude of the reversed flux wings are relatively small, as indicated by the difference in scales used for positive and negative values in Fig. 18. The ratio of the positive to negative parts of  $F$  in the historical geomagnetic field is only about 10%, which is about one half as large as the precursor in non-reversing collapse *II*, and about one quarter as large as the reversal precursor in case *I*. By this measure, the geomagnetic field does not seem to be on a reversing trajectory as of now.

The solid and dashed curves in Fig. 18 show the evolution of the rms dipole intensity and the rms field intensity on the core–mantle boundary during the 150-year period. Although the dipole decrease is monotonic, there are variations in its rate, and the most vigorous development of reverse flux patches coincides with times of most rapid dipole decrease. Gubbins et al. (2006) argued that the present-day phase of dipole decrease actually began around 1840 with the first appearance of this crop of reversed flux patches. Meanwhile the rms field strength on the core–mantle boundary has changed relatively little, as pointed out by Benton and Voorhies (1987), and may have actually increased slightly between 1920 and 1950. At the present time, for example, the instantaneous rate of change of the rms field on the core–mantle boundary is around  $-3\%$  per century equivalent, based on the POMME-4 field model expanded to degree  $l = 8$ , or  $+4\%$  per century, based on the same model expanded to degree  $l = 14$ .

Qualitatively, these trends in the rms field and dipole intensities on the core–mantle boundary suggest the early stage of dipole collapse seen in Fig. 14, when  $B_d$  begins its rapid decrease before  $B_0$  does. Near conservation of the total core–mantle boundary flux in the face of a rapidly decreasing dipole moment is characteristic of a transient magnetic energy cascade, where the initial reduction in dipole intensity on the outer boundary is partially compensated by increases in the intensity of progressively higher multipole fields. Although this is not conclusive evidence, the overall behavior of present-day geomagnetic field on the core–mantle boundary is consistent with a geodynamo mixing event.

Interpreting dipole collapses as mixing events has significant implications for the geodynamo. A mixing event involves time-variable convection with reduced equatorial symmetry, that re-arranges the internal magnetic field, inducing or strengthening reversed flux ropes and producing reversed magnetic flux on the boundary. Whether or not a such an event produces a polarity reversal depends on the duration and severity of the dipole collapse, plus the amount of field variability at the height of the collapse, particularly the variability of the equatorial dipole. Larger doses of these ingredients favor reversals, so according to our model, the stronger and more sustained the mixing event, the more likely a polarity reversal will result. Observable symptoms of mixing in the outer core include emergence of mid- and high latitude reversed flux patches and a wave number cascade of the geomagnetic field on the core–mantle boundary. We have also identified a possible reversal precursor based on the ratio of reversed to normal contributions to the axial dipole. Our analysis of the historical geomagnetic field indicates that the reversed flux now on the core–mantle boundary would have to triple or quadruple its effect on the axial dipole in order to reach the reversal precursor criterion inferred from the dynamo model.

Portions of this model are testable, especially in the current era of high-resolution and high-precision global geomagnetic field measurements. Amit and Olson (2008) analyzed geomagnetic

dipole tilt changes in terms of magnetic field transport mechanisms, and found that the large-scale core flow must be variable on decade time scales in order to account for the recent, rapid decrease in the dipole tilt angle by frozen flux advection. Olsen and Mandea (2008) modeled the secular variation of the satellite-derived core field since 1999 in terms of frozen flux and found evidence for even shorter-term changes in the core flow, on time scales of months. Geomagnetic jerks (Courillot and LeMouél, 1984; Bloxham et al., 2002; Dormy and Mandea, 2005) are yet another class of transient secular variation phenomena that may possibly have their origin in dynamo mixing. Finally, we have pointed to some preliminary evidence suggesting that geomagnetic energy is cascading from the dipole to higher field harmonics, an effect which could be verified with longer-term, and higher resolution images of the core field.

## Acknowledgements

We gratefully acknowledge support for P.O. and P.D. through grant EAR-0604974 from the Geophysics Section of the National Science Foundation, and support for H. A. from the InterEuropean Marie Curie Action. Insightful comments from two anonymous referees are greatly appreciated.

## References

- Amit, H., Aubert, J., Hulot, G., Olson, P., 2008. A simple model for mantle-driven flow at the top of Earth's core. *Earth Planets Space* 60, 845–854.
- Amit, H., Olson, P., 2006. Time-average and time-dependent parts of core flow. *Phys. Earth Planet. Inter.* 155, 120–139.
- Amit, H., Olson, P., 2008. Geomagnetic dipole tilt changes induced by core flow. *Phys. Earth Planet. Inter.* 166, 226–238.
- Aubert, J., Amit, H., Hulot, G., Olson, P., 2008a. Thermo-chemical wind flows couple Earth's inner core growth to mantle heterogeneity. *Nature* 454, 758–761.
- Aubert, J., Aurnou, J., Wicht, J., 2008b. The magnetic structure of convection-driven numerical dynamos. *Geophys. J. Int.* 172, 945–956.
- Benton, E.R., Voorhies, C.V., 1987. Testing recent geomagnetic field models via magnetic flux conservation at the core–mantle boundary. *Phys. Earth Planet. Inter.* 48, 350–357.
- Bloxham, J., 1986. The expulsion of magnetic flux from the Earth's core. *Geophys. J. R. Astr. Soc.* 87, 669–678.
- Bloxham, J., 2002. Time-independent and time-dependent behaviour of high latitude flux bundles at the core–mantle boundary. *Geophys. Res. Lett.* 29, 1854–1857.
- Bloxham, J., Zatman, S., Dumberry, M., 2002. The origin of geomagnetic jerks. *Nature* 420, 65–68.
- Bogue, S.W., Paul, H.A., 1993. Distinctive field behavior following geomagnetic reversals. *Geophys. Res. Lett.* 20, 2399–2402.
- Christensen, U.R., Aubert, J., Cardin, P., Dormy, E., Gibbons, S., Glatzmaier, G.A., Grote, E., Honkura, Y., Jones, C., Kono, M., Matsushima, M., Sakuraba, A., Takahashi, F., Tilgner, A., Wicht, J., Zhang, K., 2001. A numerical dynamo benchmark. *Phys. Earth Planet. Inter.* 128, 25–34.
- Christensen, U.R., Aubert, J., 2006. Scaling properties of convection-driven dynamos in rotating spherical shells and application to planetary magnetic fields. *Geophys. J. Int.* 166, 97–114.
- Christensen, U.R., Wicht, J., 2007. Numerical Dynamo Simulations. In: Olson, P. (Ed.), *Treatise on Geophysics*, vol. 8. Elsevier B.V., pp. 245–282.
- Clement, B.M., 2004. Dependence of the duration of geomagnetic polarity reversals on site latitude. *Nature* 428, 637–640.
- Coe, R., Glatzmaier, G., Roberts, P.H., 2000. An examination of simulated geomagnetic reversals from a palaeomagnetic perspective. *Phil. Trans. Roy. Soc. Lond.* A358, 1141–1170.
- Constable, C.G., 2003. Geomagnetic reversals: rates, timescales, preferred paths, statistical models and simulations. In: Jones, C.A., Soward, A.M., Zhang, K. (Eds.), *Earth's Core and Lower Mantle*. Taylor and Francis, London, pp. 77–99.
- Constable, C.G., Korte, M., 2006. Is Earth's magnetic field reversing? *Earth Planet. Sci. Lett.* 246, 1–16.
- Constable, C.G., Parker, R.L., 1988. Statistics of geomagnetic secular variation for the past 5 m.y. *J. Geophys. Res.* 93, 11569–11581.
- Constable, C., Johnson, C., 2005. A paleomagnetic power spectrum. *Phys. Earth Planet. Inter.* 153, 61–73.
- Courillot, V., LeMouél, J.-L., 1984. Geomagnetic secular variation impulses. *Nature* 311, 709–716.
- Cox, A., 1975. Reversed flux as reversal mechanism. *Rev. Geophys. Space Phys.* 13, 35–51.
- Dormy, E., Mandea, M., 2005. Tracking geomagnetic impulses at the core–mantle boundary. *Earth Planet. Sci. Lett.* 237, 300–309.
- Driscoll, P., Olson, P., submitted for publication. Effects of buoyancy and rotation on the reversal frequency of gravitationally-driven dynamos.
- Glatzmaier, G.A., 2002. Dynamo models: how realistic are they? *Annu. Rev. Earth Planet. Sci.* 30, 237–257.

- Glatzmaier, G.A., Roberts, P.H., 1995. A three-dimensional self-consistent computer simulation of a geomagnetic field reversal. *Nature* 377, 203–208.
- Glatzmaier, G.A., Coe, R.S., 2007. Magnetic Reversals in the Core. In: Olson, P. (Ed.), *Treatise on Geophysics*, vol. 8. Elsevier B.V., pp. 283–299.
- Glatzmaier, G.A., Coe, R.S., Hongre, L., Roberts, P.H., 1999. The role of the Earth's mantle in controlling the frequency of geomagnetic reversals. *Nature* 401, 885–890.
- Gubbins, D., 1987. Mechanisms of geomagnetic polarity reversals. *Nature* 326, 167–169.
- Gubbins, D., Jones, A.L., Finlay, C.C., 2006. Fall in Earth's magnetic field is erratic. *Science* 312, 900–902.
- Gubbins, D., Willis, A.P., Sreenivasan, B., 2007. Correlation of Earth's magnetic field with lower mantle thermal and seismic structure. *Phys. Earth Planet. Inter.* 162, 256–260.
- Jones, C.A., 2007. Thermal and compositional convection in the core. In: Olson, P. (Ed.), *Treatise on Geophysics*, vol. 8. Elsevier B.V., pp. 131–186.
- Jackson, A., 2003. Intense equatorial flux spots on the surface of the Earth's core. *Nature* 424, 760–763.
- Jackson, A., Jonkers, A.R.T., Walker, M.R., 2000. Four centuries of geomagnetic secular variation from historical records. *Philos. Trans. R. Soc. Lond.* 358, 957–990.
- Kageyama, A., Miyagoshi, T., Sato, T., Formation of current coils in geodynamo simulations, *Nature* 454, 1106–1109, doi:10.1038/nature07227, 2008.
- Korte, M., Constable, C.G., 2005. Continuous geomagnetic field models for the past 7 millennia: 2. CALS7K. *Geochem. Geophys. Geosystem.* 6, doi:10.1029/2004GC000801.
- Kutzner, C., Christensen, U.R., 2000. Effects of driving mechanisms in geodynamo models. *Geophys. Res. Lett.* 27, 29–32.
- Kutzner, C., Christensen, U.R., 2002. From stable dipolar to reversing numerical dynamos. *Phys. Earth Planet. Inter.* 131, 29–45.
- Kutzner, C., Christensen, U.R., 2004. Simulated geomagnetic reversals and preferred virtual geomagnetic pole paths. *Geophys. J. Int.* 157, 1105–1118.
- Loper, D.E., 2007. Turbulence and small-scale dynamics in the core. In: Olson, P. (Ed.), *Treatise on Geophysics*, vol. 8. Elsevier B.V., pp. 187–206.
- Lund, S., Stoner, J.S., Channell, J.E.T., Acton, G., 2006. A summary of Brunhes paleomagnetic field variability recorded in ocean drilling program cores. *Phys. Earth Planet. Inter.* 156, 194–204.
- Maunder, E.W., 1913. Distribution of sunspots in heliographic latitude 1874. *Mon. Not. Roy. Astron. Soc.* 74, 112–116.
- Maus, S., Lühr, H., Balasis, G., Rother, M., Manda, M., 2005. Introducing POMME, the Potsdam Magnetic Model of the Earth. In: Reigber, C., Lühr, H., Schwintzer, P., Wickert, J. (Eds.), *Earth Observation with CHAMP*. Springer, Berlin-Heidelberg, pp. 293–298.
- McDonald, K.L., Gunst, R.H., 1968. Recent trends in the earth's magnetic field. *J. Geophys. Res.* 73, 2057–2067.
- Merrill, R.T., McFadden, P.L., 1999. Geomagnetic polarity transitions. *Rev. Geophys.* 37, 201–226.
- Moffatt, H.K., 1978. *Magnetic Field Generation in Electrically Conducting Fluids*. Cambridge University Press, Cambridge, U.K.
- Nishikawa, N., Kusano, K., 2008. Simulation study of symmetry-breaking instability and the dipole field reversal in a rotating spherical shell dynamo. *Phys. Plasmas* 15, 082903.
- Olsen, N., Manda, M., 2008. Rapidly changing flows in the Earth's core. *Nature Geoscience* 1, 390–394, doi:10.1038/ngeo203.
- Olson, P., 2007. Gravitational dynamos and the low frequency geomagnetic secular variation. *Proc. Nat. Acad. Sci.* 104, 20159–20166.
- Olson, P., Amit, H., 2006. Changes in earth's dipole. *Naturwissenschaften* 93, 11519–11542.
- Olson, P., Christensen, U.R., 2006. Dipole moment scaling for convection-driven planetary dynamos. *Earth Planet. Sci. Lett.* 250, 561–571.
- Ossendrijver, M., 2003. The solar dynamo. *Astron. Astrophys. Rev.* 11, 287–367.
- Rotvig, J., submitted for publication. An investigation of reversing numerical dynamos driven by either differential or volumetric heating. *Phys. Earth Planet. Inter.*
- Sarson, G.R., Jones, C.A., 1999. A convection driven geodynamo reversal model. *Phys. Earth Planet. Inter.* 111, 3–20.
- Stacey, F.D., 1992. *Physics of the Earth*, 3rd ed. Brookfield Press, Brisbane, AU.
- Takahashi, F., Matsushima, M., Honkura, Y., 2005. Simulations of a quasi-Taylor state geomagnetic field including polarity reversals on the Earth Simulator. *Science* 309, 459–461.
- Takahashi, F., Matsushima, M., Honkura, Y., 2007. A numerical study on magnetic polarity transition in an MHD dynamo model. *Earth Planets Space* 59, 665–673.
- Takahashi, F., Matsushima, M., Honkura, Y., 2008. Scale variability in convection-driven MHD dynamos at low Ekman number. *Phys. Earth Planet. Inter.* 167, 168–178.
- Tauxe, L., Yamazaki, T., 2007. Paleointensities. In: Kono, M. (Ed.), *Treatise on Geophysics*, vol. 5. Elsevier B.V., pp. 509–563.
- Ternullo, M., 2007. The butterfly diagram fine structure. *Solar Phys.* 240, 153–164.
- Valet, J.P., Herrero-Bervera, H., 2003. Some characteristics of geomagnetic reversals inferred from detailed volcanic records. *Compt. Rend. Geoscience* 335, 79–90.
- Valet, J.P., 2003. Time variations in geomagnetic intensity. *Rev. Geophys.* 41 (1), 1004, doi:10.1029/2001RG000104.
- Valet, J.P., Meynadier, L., Guyodo, Y., 2005. Geomagnetic dipole strength and reversal rate over the past two million years. *Nature* 435, 802–805.
- Wicht, J., 2005. Palaeomagnetic interpretation of dynamo simulations. *Geophys. J. Int.* 162, 371–380.
- Wicht, J., Olson, P., 2004. A Detailed study of the polarity reversal mechanism in a numerical dynamo model. *Geochem. Geodyn. Geosyst.* 5, doi:10.1029/2003GC000602.
- Willis, A.P., Sreenivasan, B., Gubbins, D., 2007. Thermal core–mantle interaction: exploring regimes for 'locked' dynamo action. *Phys. Earth Planet. Inter.* 165, 83–92.
- Yang, S., Odah, H., Shaw, J., 2000. Variations in the geomagnetic dipole moment over the last 12,000 years. *Geophys. J. Int.* 140, 158–162.